

# TREX-DM: a low-background Micromegas-based TPC for low-mass WIMP detection

F.J. Iguaz<sup>a</sup>, J.G. Garza<sup>b</sup>, F. Aznar<sup>c</sup>, J.F. Castel, S. Cebrián, T. Dafni,  
J.A. García, I.G. Irastorza, A. Lagraba, G. Luzón, A. Peiró

<sup>1</sup>Grupo de Física Nuclear y Astropartículas, Universidad de Zaragoza, C/ Pedro Cerbuna 12, 50009, Zaragoza, Spain.

Received: date / Accepted: date

**Abstract** If Dark Matter is made of Weakly Interacting Massive Particles (WIMPs) with masses below 10-20 GeV, the corresponding nuclear recoils in mainstream WIMP experiments are of energies too close, or below, the experimental threshold. New detection techniques, focused on the use of light target nuclei together with low energy thresholds, are needed to get competitive sensitivity to the low-mass range of the WIMP parameter space. Gas Time Projection Chambers (TPCs) can be operated with a variety of target elements, and on account of the amplification in gas, very low thresholds are achievable. Recent advances in electronics and in novel radiopure TPC readouts, especially micro-mesh gas structure (Micromegas) are improving the scalability and low-background prospects of Micromegas-based TPCs. If we add their well-known tracking capabilities, they are a good detection option for the search of low-mass WIMPs. Here we present TREX-DM, a prototype built to test this concept. The detector is designed to host an active mass of  $\sim 0.300$  kg of Ar at 10 bar, or alternatively  $\sim 0.160$  kg of Ne at 10 bar, with an energy threshold below 0.4 keVee, and is fully built with radiopure materials. We will describe the detector in detail, as well as the results from the commissioning phase on surface, and the results from a preliminary background model. The anticipated sensitivity of this technique may go beyond current experimental limits for WIMPs of masses of 2–8 GeV.

**Keywords** Dark Matter · Underground physics · Time Projection Chamber · Micromegas · Simulation

<sup>a</sup>e-mail: iguaz@unizar.es

<sup>b</sup>e-mail: jgraciag@unizar.es

<sup>c</sup>Present Address: Centro Universitario de la Defensa, Universidad de Zaragoza, Crta. de Huesca s/n, 50090, Zaragoza, Spain

## 1 Introduction

There is nowadays compelling evidence, from cosmology and astrophysics, that most of the matter of the Universe is in the form of non-baryonic cold Dark Matter (DM) [1]. The particle physics nature of this matter, however, remains a mystery. The Weakly Interacting Massive Particle (WIMP) is a good generic candidate to compose the DM. In addition, WIMPs appear naturally in well-motivated extensions of the Standard Model, in particular those including SuperSymmetry (SUSY) [2].

If our galactic DM halo is made of WIMPs, they could interact with nuclei and produce detectable nuclear recoils in the target material of underground terrestrial experiments. Due to the extreme low rate and low energy of those events, the experimental challenge in terms of background rate, threshold and target mass is formidable. During the last 30 years an ever growing experimental activity has been devoted to the development of detection techniques that have achieved increasingly larger target masses and lower levels of background, in the quest of reaching higher sensitivity to DM WIMPs. At the moment, the leading experiments in the “WIMP race” are those using relatively heavy target nuclei (e.g. Xe or Ge) –to exploit the  $A^2$  coherence in the WIMP-nucleus interaction– and using detection techniques that provide nuclear recoil discrimination. This is the case, e.g. of liquid Xe double-phase detectors (e.g. LUX [3] or XENON [4]) or hybrid Ge bolometers (like CDMS/SuperCDMS [5–7]). These experiments are currently operating, or aiming at, target masses already at the few hundreds of kilograms range, with background levels of a few counts per year per 100 kg target mass. More specifically, and just as illustrative examples, SuperCDMS [7] has operated  $\sim 9$  kg of Ge target mass with only 11 nuclear-recoil candidate

events in 577 kg-days, while plans to jump to the 100 kg scale are ongoing; in its turn, LUX [3] has already operated 250 kg of liquid Xe (of which 118 are in the fiducial volume) during 85.3 live days and a background level that effectively limits a possible WIMP signal to only 2 to 5 (depending on the mass) nuclear recoils, and corresponding to an upper limit on the WIMP-nucleon cross-section of  $7.6 \times 10^{46} \text{ cm}^2$  at a WIMP mass of 33 GeV. Such impressive numbers are obtained as a result of the availability of discrimination techniques that allow distinguishing –with some efficiency– electron recoils (produced e.g. by gammas) from the signal-like nuclear recoils. This happens because the different ionization density of nuclear and electron types of events leads to a different yields-ratio in the detection medium (ionization/scintillation in the case of noble liquids, and ionization/phonon in case of hybrid Ge bolometers). However, this discrimination capability is energy-dependent and for very low energies (typically few keV) it disappears, setting the effective threshold of the experiment.

WIMP searches are conventionally and somewhat simplistically expressed in the two-dimensional effective parameter space  $(\sigma_N, M_W)$ , where  $\sigma_N$  is the WIMP-nucleon interaction cross section and  $M_W$  is the WIMP mass. This representation usually comes with a number of additional oversimplifying assumptions, e.g., that the velocity distribution of WIMPs in the galactic halo follows a Maxwellian distribution, or that WIMPs interact exclusively (or mainly) with nuclei via elastic coherent spin-independent scattering. Although this conventional scenario is appealing to set a common ground for inter-comparison of experimental sensitivities, one has to keep in mind the implied assumptions, for many of which there is no real justification.

The large majority of the experimental effort so far has focused on the search for WIMPs of relatively large masses (of around 50 GeV and larger). This is mainly because of theoretical considerations set in the early days of WIMP searches, that identified the WIMP with the neutralino of (minimal) SUSY extensions of the Standard Model, and interpreted the early accelerator limits under the light of these models. The establishment of this “WIMP orthodoxy” (as it is called in [8]) was facilitated by the fact that the best WIMP detection techniques available were already well suited for this mass range. Indeed, mainstream experiments show the best sensitivity for  $M_W \sim 50 \text{ GeV}$ , partially due to the kinematical matching between the WIMP and the nuclear mass. For higher masses the sensitivity to  $\sigma_N$  slowly decreases, while for lower masses it gets sharply reduced because of the effect of the energy threshold.

Despite the enormous progress in WIMP experiments during the last 10-15 years, that has witnessed

an improvement in sensitivity to  $\sigma_N$  of more than 4 orders of magnitude, no conclusive WIMP positive signal has been seen so far. This fact has triggered the revision of the mentioned assumptions and the study of more generic phenomenological WIMP frameworks (other WIMPs interactions, different WIMP velocity distributions, etc.). Besides, the non-observation of signals of SUSY in the last run of the Large Hadron Collider (LHC) calls also for adopting more open-minded views of the possible theoretical frameworks behind the WIMP paradigm. With these facts in mind, recent theoretical and phenomenological efforts have focused on the study of less conventional SUSY models, or even non-SUSY WIMP models (like e.g. Asymmetric DM models [9]).

### 1.1 Low-mass WIMPs

As part of this view of going beyond the WIMP orthodoxy, some recent experimental and phenomenological efforts have been focused on the study of WIMPs in the low-mass range (i.e.  $M_W < 10 - 20 \text{ GeV}$ ). The interest on this region of the parameter space, traditionally out of reach of mainstream experiments, was increased by the appearance of a number of hints that could be interpreted as collisions of low-mass WIMPs [10–12] (although those interpretations seem to have weakened over time [7, 13]). In addition, the well-known and persistent DAMA/LIBRA claim [10], incompatible with results from other experiments in conventional scenarios, might be reconciled only within very non-standard model assumptions, some of them invoking low-mass WIMPs [14]. Independently of the weight one gives to those hints, or to the theoretical motivation of low-mass WIMPs, it is clear that in the present situation of WIMP searches, as much as it is important to extend the current generic  $(\sigma_N, M_W)$  sensitivity front-line to lower  $\sigma_N$  values, so is it to extend it to lower  $M_W$  values too.

On more experimental grounds, sensitivity to low-mass WIMPs poses particular challenges. As mentioned above, mainstream experiments are severely limited at low-masses due to the threshold effect of the nuclear recoil discrimination capabilities. Despite the impression that sensitivity lines may progress towards low-masses as long as larger target masses are gathered (see e.g. LUX exclusion plot in Fig. 21) this needs to be taken with a lot of caution. Low-mass WIMPs leave energy deposits typically below the energy threshold of experiments based on heavy target nuclei like Xe or Ge. This means that the exclusion limits derived for low-mass WIMPs by these experiments rely on a very small (1%

or lower) fraction of the WIMP interactions in the detector, those corresponding to the high velocity tail of the distribution (with kinetic energies high enough to produce a nuclear recoil visible in the detector). But precisely this part of the distribution is the most uncertain, and in some plausible galactic halo models (i.e. those with lower maximum WIMP velocity) it can altogether disappear. It is clear that to tackle the low-mass WIMP region, specific experiments optimized for this mass range are needed. A robust detection or exclusion must imply that a substantial fraction (order 50%) of the WIMP spectrum is over the experimental threshold. To achieve this the use of light target nuclei is preferred (to kinematically reach higher recoil energies), as well as techniques with intrinsically low energy detection threshold. These requirements are incompatible with the discrimination between nuclear and electron recoils, whose distinctive features become blurred at low energies. Some experimental efforts (still at modest scales) are already being carried out in this direction. Some conventional experiments, like e.g. CDMS [6] or XENON [15], have developed an analysis specifically for low energy data, bypassing their nuclear/electron discrimination and going to lower thresholds. More relevantly, first experiments specifically focused on the new low-mass WIMP paradigm in the way exposed above are already appearing, like DAMIC [16], CDEX [17], or CDMSlite [18] among others. As the background levels in these experiments must rely on more conventional handles like e.g. ultra-high levels of radiopurity of the detector components, the scale of these experiments remain so far at a relatively modest scale (still below the kg level of target mass).

## 1.2 High pressure TPCs to search for low-mass WIMPs

In this paper we propose the use of gas Time Projection Chambers (TPCs) with novel Micromegas readouts to search for low-mass WIMPs. Being gaseous detectors, the scaling-up prospects of gas TPCs are typically considered modest. However, advances in electronics and novel micro-pattern gas readout planes (especially Micromegas) are changing this view. The objective of the T-REX project [19, 20] is to study the applicability of Micromegas readouts TPCs to rare event searches (not just to WIMP searches, but also axions [21] and double beta decay [22]). The T-REX activity<sup>1</sup> during the last years has included the study and characterization of novel Micromegas readouts [23], especially those of microbulk type [24], study and improvement of their ra-

diopurity [25], simulation and development of discrimination algorithms [26], and the construction and test of demonstrating prototypes [21, 27–30]. It is our claim here that the charge amplification inherent to gaseous detectors (yielding correspondingly low threshold) and the flexibility in the choice of target gas (and pressure), together with the aforementioned advances in radiopurity, scaling-up and general simplification of these detectors, make them very promising options for low-mass WIMP detection.

As part of the T-REX project, a prototype to assess the feasibility of a low-mass WIMP detector with this technique has been developed: TREX-DM. This paper constitutes the first detailed presentation of this activity, its current status and prospects. In Sec. 2 a technical description of the TREX-DM prototype is made. Section 3 is devoted to the first experimental results of the commissioning in surface, focused on performance results of the Micromegas readout planes. In Sec. 4 we review the radiopurity results of the detector components, a very important aspect of the project. Based on these, in Sec. 5 we introduce a preliminary background model for the detector, with which we tentatively assess the physics prospects in Sec. 6. The conclusions and the outlook (Sec. 7) complete this paper.

We must note here that another important reason why gas TPCs are being considered as WIMP detectors is because they could provide access to the imaging of the nuclear recoils, and therefore to the WIMP incoming direction [31]. WIMP directionality is considered the ultimate signature to unambiguously identify the extraterrestrial origin of a putative signal. The experimental challenge is big, due to the tiny size of nuclear recoils, and it requires working at very low pressure and with very high granularity readouts. Apart from the pioneer DRIFT experiment [32], a number of more recent initiatives are ongoing to demonstrate directional sensitivity with a number of different TPC prototypes, like MIMAC [33], NEWAGE [34], DMTPC [35] and others. Although we acknowledge the importance of this goal as a motivation to develop gas TPCs for WIMP searches, TREX-DM is focused in the non-directional detection of WIMPs. This allows, among other things, to operate at high pressure in order to increase exposure.

## 2 Description of the experimental setup

The TREX-DM detector is conceived to host 0.3 kg of Ar target mass at 10 bar (or, alternatively, 0.16 kg of Ne). In some respects, the detector is a scaled-up version of the low-background Micromegas x-ray detectors developed for axion research [21], but with a  $10^3$  times larger active mass. The detector is built taking into

<sup>1</sup>T-REX webpage: <http://gifna.unizar.es/trex/>

account state-of-the-art radiopurity specifications, for which a dedicated campaign of material identification and measurements has been carried out (see Sec. 4). In the present version of the detector, to be described in the following, a few components are not yet the most radiopure ones and will be replaced for the physics run in underground operation, as is discussed in Sec. 2.6.

## 2.1 Vessel and shielding

The vessel is composed of a forged and machined Electrolytic Tough Pitch Copper (ETP Cu) sleeve, with a 0.5 m diameter and 0.5 m length and two 6 cm thick Oxygen Free Electronic Copper (OFE Cu) machined flat end caps. Its thickness (6 cm) is enough to both hold pressures up to 12 bar and be part of the passive shielding of external backgrounds. The vessel is supported at the present time by an aluminum frame, which allows the separation of the two caps from the central body. In this way, the readout planes and the drift cage can be independently mounted.

## 2.2 Active volume symmetrical distribution

The inner volume of the vessel is divided into two active volumes (Fig. 1, a), separated by a central cathode (b). This cathode consists of a squared copper frame, on which a 4  $\mu\text{m}$  aluminized mylar foil is glued. The cathode is electrically isolated from the vessel by a teflon gasket, which prevents any spark at voltages up to 40 kV. It is connected to a tailor-made high voltage feedthrough (c), composed by a ETP Cu round bar inserted in a machined teflon rod that also works as gasket for sealing purposes (d). Around each active volume, there is a 19 cm long and 25 cm side square sectioned field cage (d), composed of a copper-kapton printed circuit. Each circuit is screwed to four teflon walls with the aim to electrically isolate the supported printed circuits and at the same time shield the active volume from the inner walls of the copper vessel. The copper strips are 1 mm thick, are separated 7 mm and are electrically linked one after the other by 10 M $\Omega$  resistors<sup>2</sup>. The inner drift chain ends at each side at a 1 mm thick copper squared ring, also covered by a teflon gasket to prevent from sparks damaging the readout plane frame. This last ring is connected via a cable<sup>3</sup> to a customized high voltage feedthrough, made of a copper bar glued to a copper flange by epoxy Hysol<sup>4</sup> (e). Its voltage is adjusted by an external variable resistor

<sup>2</sup>SM5D resistor, produced by Finechem.

<sup>3</sup>AWG 18/19/30, produced by Druffon.

<sup>4</sup>Hysol RE2039, produced by Henkel.

(connected to ground) in order to have an homogeneous drift field independently on the voltage applied to the central cathode<sup>5</sup> and the Micromegas mesh<sup>6</sup>.

## 2.3 Micromegas readout planes

The Micromegas anode planes (Fig. 1, f; and Fig. 2) are a modified version of those used in CAST [21]. Each readout plane is on a circular Printed Circuit Board (PCB, made by Somacis) of 375 mm diameter and 1.6 mm thickness, whose core materials are FR4/phenolic and copper (17  $\mu\text{m}$  of thickness). The active surface is  $25.2 \times 25.2 \text{ cm}^2$ , which is divided in squared pads of 332  $\mu\text{m}$  length with a pitch of 583  $\mu\text{m}$ . The pads are alternatively interconnected in 432 strips per direction ( $X$  and  $Y$ ) through resin filled holes, which are then routed to four connectors prints at the PCB sides. A stainless-steel mesh was laminated on the PCB (creating an amplification gap of 128  $\mu\text{m}$ ) at the Saclay workshop using the bulk technology [36]. Each PCB is fixed to a circular copper base, which is then fixed to the respective cap by four copper columns. A flat cable (g) links each readout plane footprint to the electronics by means of a commercial 300-pin solderless connector<sup>7</sup> (h). The connectivity is assured by four screws, which also join two 1 cm thick lead covers and two 1 cm thick copper containers. These pieces are conceived to partially shield the intrinsic radioactivity of the connectors. Each flat cable goes out from the vessel through a slit at the corresponding end cap that ends in a copper feedthrough (i). The flat cable is fixed to this piece by a teflon gasket, which is then glued by epoxy Hysol. The copper feedthrough is then screwed to the end cap and its leak-tightness is assured by a teflon o-ring.

## 2.4 Readout electronics

An event interacting in either of the active volumes releases electrons, which drift towards the Micromegas readout planes. These primary electrons are then amplified in the gap and the charge movement induces signals both at the mesh and the strips. Both signals are processed by two different electronic chains, whose schema are shown in Fig. 3. The mesh signal is extracted from the vessel by a coaxial low noise cable<sup>8</sup> and a feedthrough (i) similar to the field cage ones. The signal is decoupled from the high voltage by a filter, whose characteristic  $RC$  constant minimizes the recovery time

<sup>5</sup>Powered by a Spellman SL50N30/230/LR/SIC module.

<sup>6</sup>Powered by a CAEN N470A module.

<sup>7</sup>GFZ300, produced by SAMTEC.

<sup>8</sup>SML50SCA, produced by AXON.



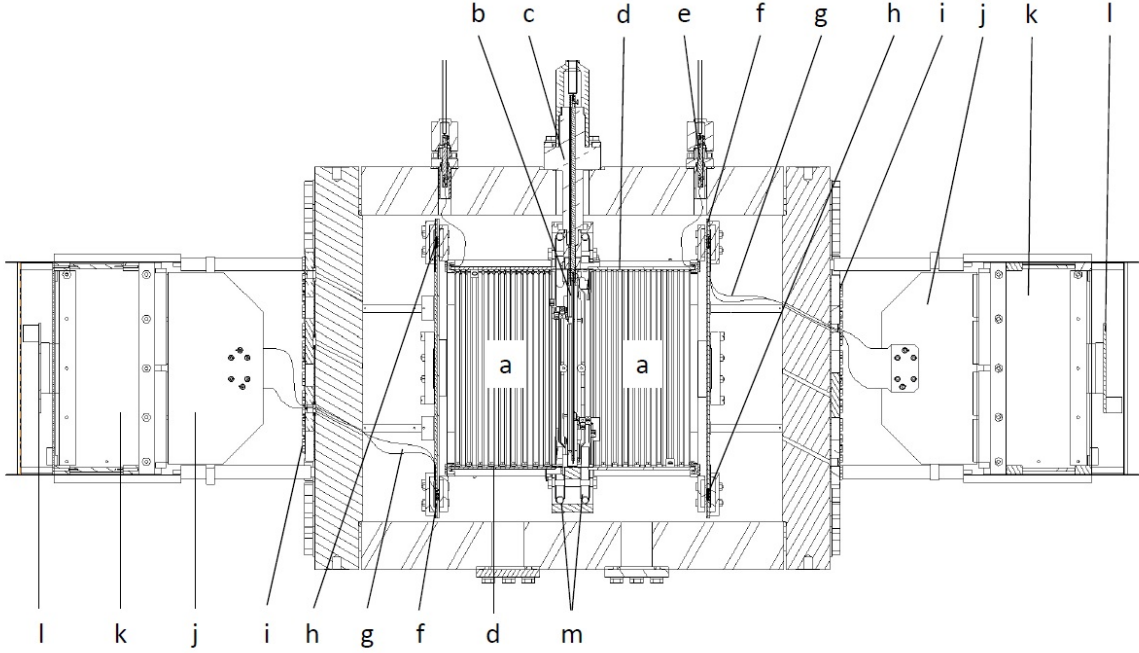


**Fig. 1** Schema of the experimental setup. The different components are described in detail in the text: active volumes (a), central cathode (b), high voltage feedthrough (c), field cage (d), *last ring* feedthrough (e), Micromegas readout planes (f), flat cable (g), Samtec connectors (h), signal feedthroughs (i), interface card (j), AFTER-based FEC (k) and FEM boards (l), and calibration tube (m).



**Fig. 2** View of one of the vessel's caps, where several components described in detail in the text are shown: a readout plane, its copper shielding pieces, its four flat cables and part of the electronics: the interface cards and the FEC cards.

after a possible current excursion produced by a spark at the amplification gap. The signal is afterwards processed by a preamplifier<sup>9</sup>, a spectroscopy amplifier<sup>10</sup>, and is subsequently recorded by a Multichannel Ana-

lyzer (MCA)<sup>11</sup>. In parallel, strip pulses come out from the vessel by four flat cables. Each of them is connected to an interface card (j), that routes the signals to the ERNI connectors of an AFTER (ASIC For TPC Electronics Readout)-based front-end card (FEC) board (k) [37, 38]. Each board has four AFTER ASICs that amplify and sample the signals continuously at 50 MHz in 512 samples per channel, corresponding to a time window of  $\sim 10 \mu\text{s}$ , which is longer than the maximum drift time of an event in an active volume. The electronics is triggered by the negative component of the mesh's amplified bipolar pulse, which passes through a discriminator<sup>12</sup> and a NIM-to-TTL adapter<sup>13</sup>, and is fed to a Data Concentrator Card (DCC)<sup>14</sup>. If a trigger arrives, the analog data from all channels is digitized by the ASICs. Then, a pure digital electronics card, the front-end mezzanine (FEM) board (l), gathers all digital data, performs a pedestal subtraction and sends it to the DCC card via optical fiber, which is connected to the computer by means of a standard network cable. The  $XZ$  and  $YZ$  views of an event are reconstructed combining the strip pulses, whose temporal position gives the relative  $z$  position, and the decoding of both

<sup>11</sup>Amptek MCA8000A.

<sup>12</sup>Lecroy 623A.

<sup>13</sup>Lecroy 688.

<sup>14</sup>Xilinx ML-405.

<sup>9</sup>Model 2004 by Canberra.

<sup>10</sup>Model 2021 by Canberra.

the readout plane and the interface card. An example of the pulses acquired by the electronics and the corresponding reconstructed event is shown in Fig. 3 (right).

As a low energy threshold is one of the main goals of the experiment, special care has been given to grounding in the electronics design: each high voltage line has a dedicated low-frequency filter to dim the signal ripples from high voltage sources; coaxial cables are used for mesh and ground connexions; signal paths are surrounded by a ground layer both at the readout plane, the flat cables and the interface cards to avoid any coupling; the AFTER-based cards (FEM and FECs) of each side are inside a Faraday cage to minimize induced noises. These Faraday cages, which were initially isolated from the vessel, were found the origin of a MHz-frequency noise. This noise was removed by covering with aluminum foil both the flat cables and the interface cards, and connecting simultaneously the Faraday cages and the vessel. This fact points to either a design issue of the interface cards or an intrinsic noise source at the level of the AFTER-based electronics, which should be solved in near-term upgrades.

## 2.5 Calibration and Gas system

The setup is equipped with more subsystems. The first one is the calibration system, which consists of a very thin aluminum holder containing a deposition of  $^{109}\text{Cd}$ . This radioactive source emits x-rays of 22.1 ( $K_\alpha$ ) and 24.9 keV ( $K_\beta$ ). The holder is screwed to a 3 mm diameter nylon wire, which slides in a teflon tube located inside the vessel (Fig. 1, m) through a leak tight port at the bottom part. The rod can be manually moved to four calibration points per active volume, situated at the corners of the central cathode, where the source illuminates directly the two active volumes. In addition, there are two ports situated at the bottom (inlet) and the top (outlet), where gas enters and comes out from the vessel. The gas comes from a premixed bottle, whose pressure is adjusted by a pressure transducer<sup>15</sup> and whose flow is set by a mass flowmeter<sup>16</sup>. These two components, three temperature sensors, a pressure sensor<sup>17</sup> and the HV sources are continuously monitored by a slow control, programmed in Python and based on Arduino cards [39]. Finally, the vessel has a stainless steel CF40 flange through which it can be pumped before its operation to reduce the release of trapped air or other impurities from elements inside the vessel.

<sup>15</sup>F-702CV-AGD-33-V by Bronkhorst.

<sup>16</sup>F-201CV-AGD-33-V by Bronkhorst.

<sup>17</sup>PTU-F-AC15-33AG by Swagelok.

## 2.6 Required modifications for a physics run

Three main changes are planned for a physics run in an underground laboratory: the external support and shielding, the readout plane and the gas. The actual aluminum support structure should be replaced by a copper-based one, cleaner in terms of radiopurity. The structure should also be compatible with a lead shielding, to reduce the effect of the external gamma flux, and another systems will also be affected like the gas and vacuum systems, which should be made of copper near the vessel. Finally, the use of an automated calibration system will be needed to minimize the number of openings of the shielding.

About the readout plane, two materials must be replaced by clean ones, in terms of radiopurity: FR4 PCB, present at the readout plane, and Liquid Crystal Polymer, present at the connectors. Both changes are technically feasible in the near future: a Micromegas readout built only out of kapton and copper and connectors made of silicone. The improvement in terms of radiopurity is described in detail in Sec. 4. Finally, the gas should not contain any radioactive isotope. Very light gases like helium and neon normally do not have any but for instance, argon has the isotope  $^{39}\text{Ar}$ , which decays by beta-emission ( $Q = 565$  keV) and has a long half-life (239 yr). It is produced at surface level by cosmogenic activation and the best way to avoid it is extracting argon for underground sources [40].

## 3 Detector characterization at low energy

Micromegas readout planes are being characterized in argon- and neon-based mixtures at high pressure using a  $^{109}\text{Cd}$  source, in order to find an optimum point of operation (in terms of general performance and energy threshold) for a physics run. This optimization is a challenging task as it depends on many factors (the base gas, the quencher and its quantity; and the pressure) and there are few studies in literature on gas properties. For simplicity, we have started the characterization with  $\text{Ar}+2\%\text{iC}_4\text{H}_{10}$ , the gas normally used in CAST Micromegas detectors [21]. This initial choice is reasonable: isobutane gives good results in argon-based mixtures [41] and even if 2% of isobutane may be too little for atmospheric pressure [41], it is known that optimal relative quencher concentrations decrease with pressure, e.g. for Xe-TMA mixtures [42]. The results of this characterization will be presented and discussed here. We will also present some first results in  $\text{Ar}+5\%\text{iC}_4\text{H}_{10}$ , taken in better noise conditions, to estimate the actual energy threshold of TREX-DM experiment (see Sec. 3.4).

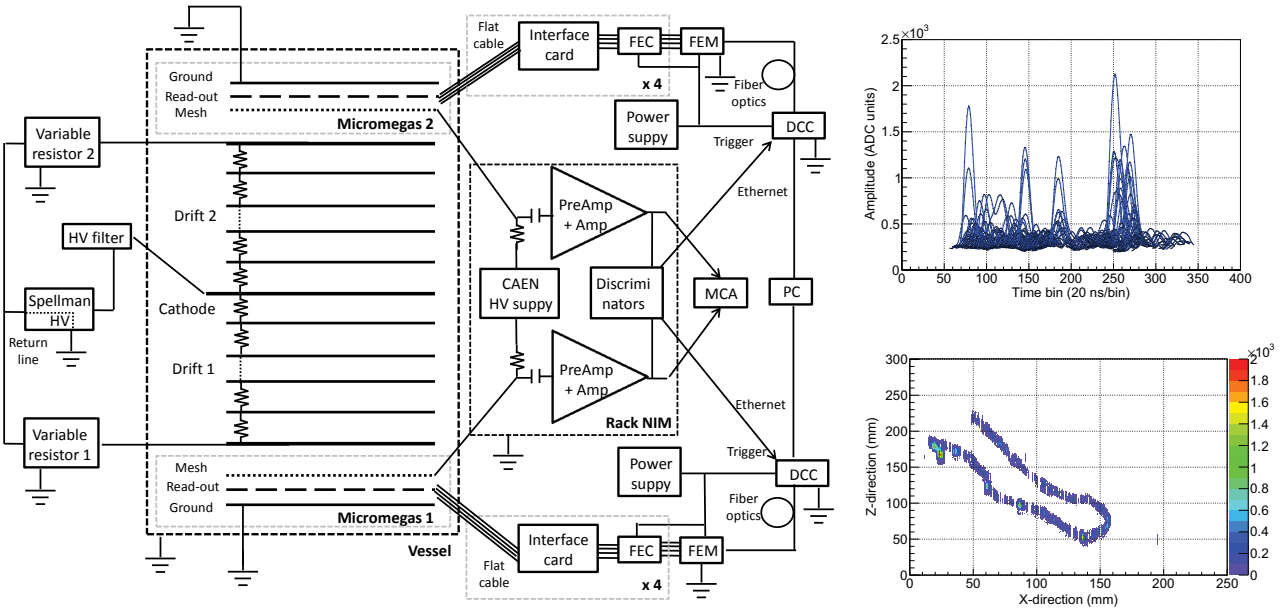


**Fig. 3** Left: A diagram of the electronic chain, which is described in detail in text. Top right: The strip pulses of an event as they are recorded in a FEC card. Bottom right: The  $XZ$  view of a reconstructed event, as obtained from previous pulses. It corresponds to an electron with a long twisted track and a final big energy deposition or blob.

The role of the quencher quantity will be further studied in the near future. A 5-10% of isobutane is normally used in bulk detectors [43, 44] but so much quencher may degrade the detector performance at high pressure. The Fano factor of isobutane, related to the energy resolution, is indeed worse than argon one (0.26 vs 0.17) [45]. Finally, neon-based mixtures will be studied, which are expected to show higher gains and a better energy resolution, as theoretically shown in [45] and practically shown in [41, 44] for Micromegas detectors.

### 3.1 The experimental procedure

The experimental procedure starts by a several-day long pumping of the vessel. Then, the leak-tightness of all the vessel feedthroughs and unions is checked by means of a Helium leak detector. All components must show a value lower than  $\sim 10^{-6}$  mbar·l/s in order to start the characterization. However, the vacuum level of the full-equipped TPC is limited by the outgassing of the inner plastic components. After  $\sim 96$  hours of continuous pumping, a level of  $3.0 \times 10^{-4}$  mbar was achieved, while the outgassing/leak rate was  $3.0 \times 10^{-4}$  mbar·l/s. These values may be improved in the future by a bake-out system. Once the leak-tightness is verified, gas is injected into the vessel at an adjustable flow and high-voltage tests are performed to verify the connectivity and the spark protection. A gas flow of of 3-5 l/h is kept during all the measurements.

Two bulk Micromegas readout planes of  $128 \mu\text{m}$  amplification gap, *MM1* and *MM2*, were installed at each side of the symmetric TPC, and were simultaneously characterized in terms of electron transmission, detector gain, gain uniformity and energy threshold. We tested them in  $\text{Ar}+2\%\text{iC}_4\text{H}_{10}$  for pressures between 1.2 and 10 bar, in steps of 1 bar. For this purpose, the two detectors were calibrated at low energies by a  $^{109}\text{Cd}$   $\gamma$ -source. The spectra are characterized by the  $K$ -peaks and the fluorescence emissions at 6.4 and 8 keV from the iron and copper components (see Fig. 4). The mean position and the width of the  $K_\alpha$  is calculated through an iterative multi-Gaussian fit, previously used in [42], including both the  $K_\alpha$  and  $K_\beta$  emission lines and their escape peaks (at 19.1 and 21.9 keV). A wide range of amplification and drift fields are scanned at each pressure, which requires a bias ranging from  $\sim 300$  V at 1.2 bar to  $\sim 900$  V at 10 bar, and from  $\sim 1.5$  kV to  $\sim 30$  kV, respectively.

### 3.2 General performance

The drift voltage is varied for a fixed mesh voltage to obtain the electron transmission curve at each pressure (Fig. 5). The detectors show a plateau of full transmission for a wide range of drift-to-amplification fields ratios at all pressures. The electron transmission drops at very low drift fields ( $\sim 50$  V/cm/bar) due to electron attachment and recombination of the primary elec-

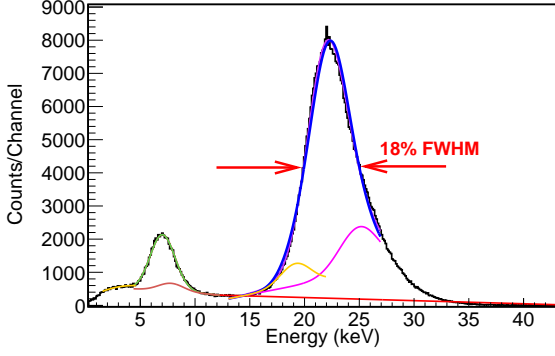


**Fig. 4** Energy spectrum generated by the mesh signals when one of the Micromegas readouts is irradiated by a  $^{109}\text{Cd}$  source in  $\text{Ar}+2\%\text{iC}_4\text{H}_{10}$  at 2 bar. The spectral parameters are defined through an iterative multi-Gaussian fit corresponding to the  $\text{K}_\alpha$  (22.1 keV, blue line) and  $\text{K}_\beta$  (24.9 keV, magenta line) emission lines of the source and their escape peaks (located at 19.1 and 21.9 keV, orange line). The fluorescence lines of iron (at 6.4 keV, emitted from the mesh) and copper (8 keV, from the vessel or the field cage strips) are also present (green and brown lines, respectively).

trons generated in the conversion volume. For high drift fields, the mesh stops being transparent for primary electrons, and the energy resolution also degrades.

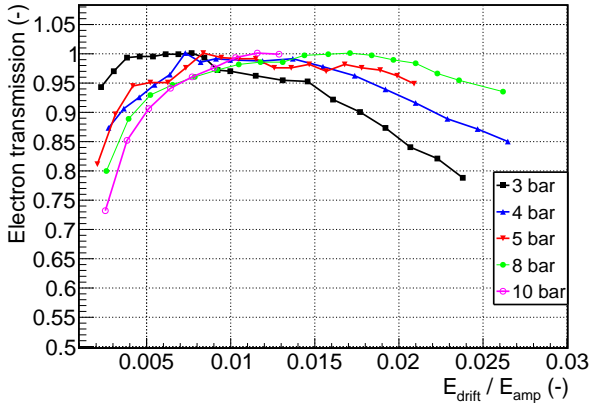


**Fig. 5** Dependence of the electron transmission with the drift-to-amplification fields ratio for the *MM2* detector in  $\text{Ar}+2\%\text{iC}_4\text{H}_{10}$  at different gas pressures. The peak positions have been normalized to the maximum of each series, assuming that the full electron transmission is always achieved.

The drift-to-amplification fields ratio is set for every pressure at the point where the mesh shows the maximum electron transmission, typically at a drift field of around 100 V/cm/bar. Then, the available range of mesh voltages is scanned, from very low amplification fields where the amplitude of the mesh signal is just above the noise threshold, up to the spark limit, where the sparking rate is too high for a safe operation. The

signal amplitude increases with the applied amplification field, while the peak position moves to higher values in the spectra. The peak position is used to calculate the absolute gain of the Micromegas readout planes, defined as the ratio of the number of electrons after the avalanche  $n$  and the number of primary electrons,  $n_0$ :  $G = \frac{n}{n_0}$ . Determining  $G$  requires the characterization of the electronic chain in order to obtain the conversion factor between the peak position registered by the MCA and the number of electrons before the preamplifier  $n$ . As described in Sec. 5.2, the number of primary electrons  $n_0$  is given by  $22.1 \text{ keV}/W_{\text{Ar}}$ , where  $W_{\text{Ar}} = 26.3 \text{ eV}$ .

The gain curves obtained in  $\text{Ar}+2\%\text{iC}_4\text{H}_{10}$  between 1.2 and 10 bar are shown in Fig. 6. The two detectors present a similar gain and in both cases, the maximum working gain before the spark limit decreases with the gas pressure, from  $3 \times 10^3$  at 1.2 bar down to  $5 \times 10^2$  at 10 bar. Both detectors reach gains higher than  $10^3$  for pressures up to  $\sim 6$  bar.

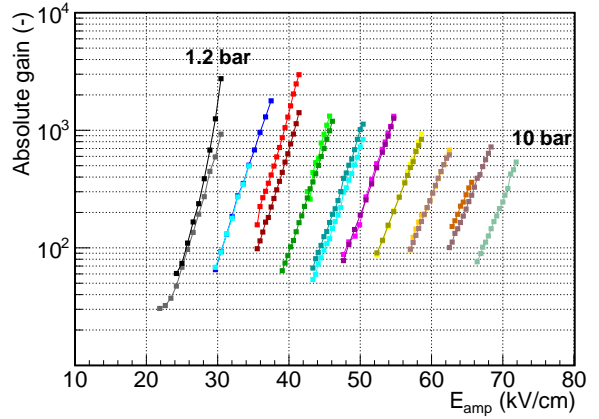


**Fig. 6** Dependence of the absolute gain with the amplification field in units of kV/cm in  $\text{Ar}+2\%\text{iC}_4\text{H}_{10}$  between 1.2 and 10 bar (in steps of 1 bar) for the *MM1* and *MM2* detectors. The maximum gain of each curve is obtained just before the spark limit.

The dependence of the energy resolution with the amplification field for all the pressures settings is shown in Fig. 7. At each pressure there is a range of amplification fields for which the energy resolution is optimized. At low gains, the energy resolution degrades because the signal becomes comparable with the noise. At high fields, the resolution degrades due to the increase in the gain fluctuations by the UV photons generated in the avalanche. As the noise conditions were not ideal, this range did not extend further to lower gains, but the best measured values may be little affected by noise level. As it is shown, the best energy resolution de-



grades with pressure, being 16% FWHM at 22.0 keV at 1.2 bar and 25% FWHM at 10 bar. These values may be limited by the low quantity of quencher (2%) in the gas. In fact, an energy resolution of 14% FWHM at 1.2 bar was measured in Ar+5% $i$ C<sub>4</sub>H<sub>10</sub> (as shown in Fig. 10). This value is closer to the best value measured by a 128  $\mu$ m-gap bulk Micromegas readout in argon-isobutane mixtures (11.9% FWHM at 22.1 keV, calculated from a 23% FWHM at 5.9 keV [43], supposing only an energy dependence).

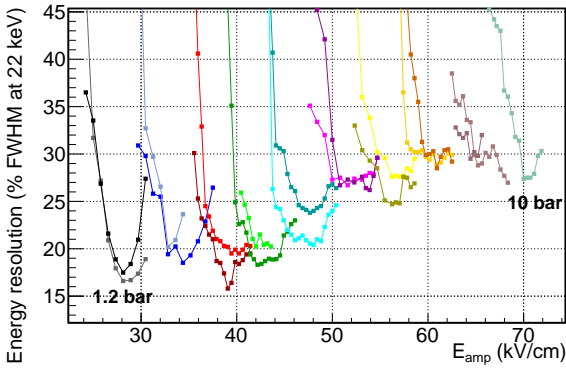


**Fig. 7** Dependence of the energy resolution at 22 keV with the amplification field for the *MM1* and *MM2* detectors of TREX-DM in Ar+2%iC<sub>4</sub>H<sub>10</sub> between 1.2 and 10 bar in steps of 1 bar. The best achievable energy resolution degrades from 16% FWHM at 1.2 bar to 25% FWHM at 10 bar. The systematic error of each point is 0.3%.

### 3.3 Gain homogeneity

The homogeneity of each detector's response was studied in Ar+2%iC<sub>4</sub>H<sub>10</sub> at 2 bar, illuminating its surface with the <sup>109</sup>Cd source at its four calibration points and using the strip signals recorded by the AFTER-based electronics. The sampling frequency was set to 50 MHz to get a temporal window of  $\sim 10 \mu$ s. In Ar+2%iC<sub>4</sub>H<sub>10</sub> at a drift field of 100 V/cm/bar, the drift velocity is 3.33 cm/ $\mu$ s, so ionization tracks as long as the active volume's length (19 cm) could be fully recorded.

Before analyzing the data, the detector surface was binned into a 2D histogram of 216 $\times$ 216 cells (each detector has 432 $\times$ 432 strips). Then, for each calibration event at the K $_{\alpha}$ -line, the mean position in  $x$ - and  $y$ -directions was calculated and its energy recorded at the corresponding  $(x, y)$  entry of the 2D histogram. Finally, each entry of the histogram was normalized by the number of x-rays registered in that bin. The resulting 2D histogram is the gain map, which is shown for both readout planes in Fig. 8. For *MM2*, the readout

response's is uniform in almost all its surface, except for two *dead strips*<sup>18</sup> in  $Y$ -direction that reduce the effective gain at two lines. The small dead area at the margins of the active area is caused by the lack of planarity of the field-cage kapton PCB. Nevertheless, its gain fluctuations are less than 10%. The *MM1* readout's response has a similar behavior, except for some more dead strips ( $\sim 20$ ) that were accidentally caused by a bad isolation of the inner mesh cable.

### 3.4 Energy threshold

In the current DAQ implementation, the trigger is built from the mesh signal. The detector threshold is thus limited by the electronic noise of the mesh channel, that is relatively high due to its high capacitance ( $\sim 6$  nF). In the final DAQ implementation planned, based on the AGET chip [46], the trigger will be generated by the very strip signals, which could easily enjoy a factor  $\sim 10$  better noise level as they show a lower capacitance ( $\sim 0.2$  nF, including the contributions of the flat cables and the interface cards). This fact is illustrated in Fig. 9, showing the strip signals of an event of 1 keV, and where the baseline fluctuations indicates that the noise threshold in the strips could be well at the level of 0.1 keV. One has to take into account that the numbers given in the following refer to noise threshold in the mesh channel, and therefore not representative of the final threshold figures of the experiment.

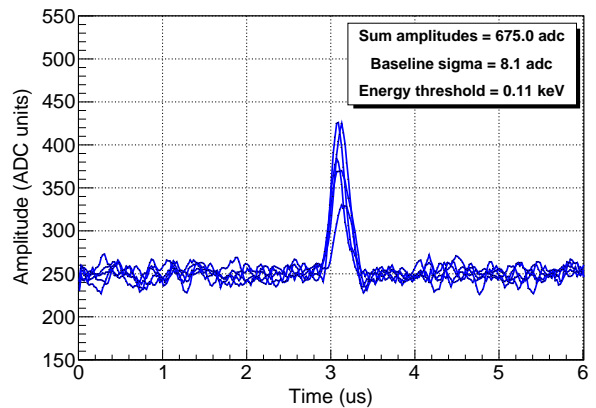


**Fig. 9** The active strip pulses of a 1 keV event, acquired by the AFTER-based electronics. The energy threshold has been estimated using the pulse baseline's sigma and the same pulse trigger level (4.0 sigma) as the one of AFTER electronics.

<sup>18</sup>A dead strip is short-circuited with the mesh. To recover the readout plane, the strip is electrically disconnected from the AFTER-based electronics at the level of the interface card by removing a resistor.

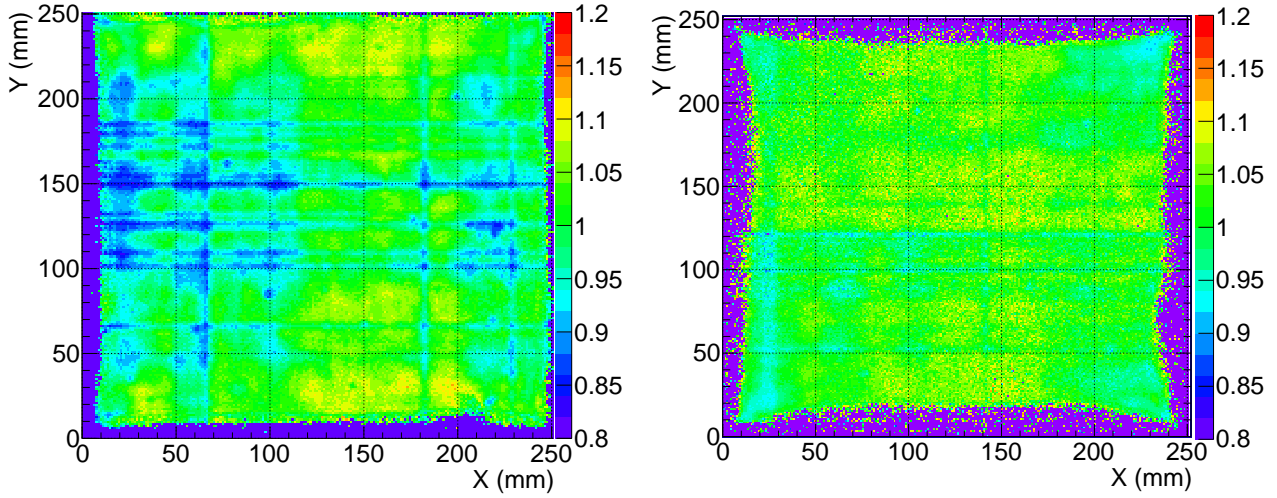


**Fig. 8** Gain uniformity of the *MM1* (left) *MM2* (right) Micromegas readout planes, generated by  $^{109}\text{Cd}$  calibrations when the vessel was filled with  $\text{Ar}+2\%\text{iC}_4\text{H}_{10}$  at 2 bar. The dead areas (in purple) show values lower than unity (in green).

The energy threshold has been defined as the lowest energy bin over the noise distribution, which follows an exponential decay at low energies. This simple definition is quite conservative as shown in Fig. 10, where the energy spectra generated by mesh and strip signals in the same conditions are compared. For each gas pressure, the minimum value was selected between the energy thresholds of all the recorded spectra, as well as its corresponding gain. This operation point was always at the optimum range of energy resolution.

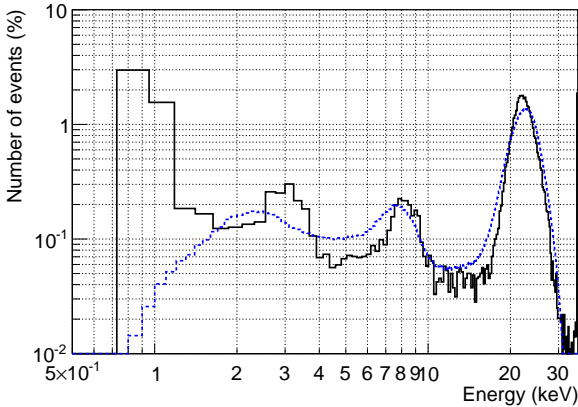


**Fig. 10** Energy spectra generated by mesh (black line) and strip signals (dashed blue line) when the *MM1* detector was irradiated by a  $^{109}\text{Cd}$  source in  $\text{Ar}+5\%\text{iC}_4\text{H}_{10}$  at 1.2 bar. The energy threshold is situated at 1.0 keVee.

The dependence of the energy threshold and its corresponding gain with pressure is shown in Fig. 11. For  $\text{Ar}+2\%\text{iC}_4\text{H}_{10}$  it degraded from 1 to 8 keV when the pressure increased from 1.2 to 10 bar, due to the reduc-

tion of the detector gain and the presence of a MHz frequency noise (see Sec. 2.4 for further details). After this noise was removed, new data in  $\text{Ar}+5\%\text{iC}_4\text{H}_{10}$  showed a smaller degradation: from 1.0 keV at 1.2 bar to 1.4 keV at 3 bar. A value of 2.8 keV at 10 bar has been conservatively estimated from this tendency.

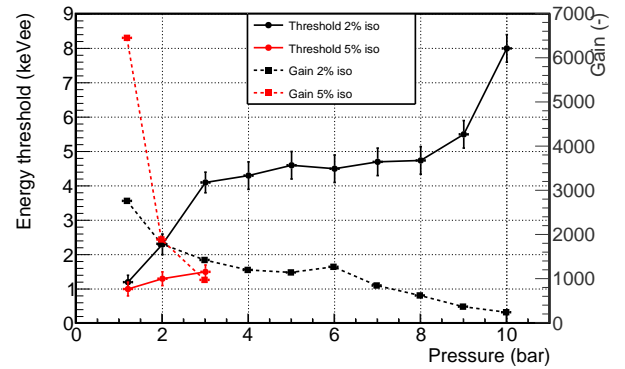


**Fig. 11** Dependence of the energy threshold (circled lines) and the operation gain (dashed squared lines) with the pressure for the *MM1* Micromegas readout plane when the vessel was filled with  $\text{Ar}+2\%\text{iC}_4\text{H}_{10}$  (black lines) and  $\text{Ar}+5\%\text{iC}_4\text{H}_{10}$  (red lines).

The best measured energy threshold (1.0 keVee) is not far from the 0.4 keVee obtained in other Micromegas detectors using the strip signals [21]. Apart from further improvements at the mesh electronics chain, a clear improvement is expected by the implementation of the AGET-based electronics. First tests of this DAQ with the IAXO-D0 prototype have shown an effective energy threshold of 100 eV [47].

## 4 Radiopurity measurements

A material screening program was undertaken to evaluate the radioactivity of all the relevant components of the detector and surrounding materials used for gas vessel, field cage, electronics or shielding, to help both in the design of the set-up and in the construction of the background model of the experiment. First results were presented in [48]. In this section, the techniques applied to carry out these measurements are described and the results obtained are shown and discussed.

The screening program is based mainly on germanium gamma-ray spectrometry performed deep underground and, complementing these results, some measurements based on Glow Discharge Mass Spectrometry (GDMS) were also carried out. GDMS was performed by Evans Analytical Group in France, providing concentrations of U, Th and K; it must be noted that having no information on daughter nuclides in the chains, a possible disequilibrium cannot be detected.

All the germanium measurements were made using a  $\sim 1$  kg ultra-low background detector of the University of Zaragoza (named *Paquito*) and operated at the hall E of the Canfranc Underground Laboratory (LSC) at a depth of 2450 m.w.e.. This detector has been used for radiopurity measurements at Canfranc for several years (details can be found in [25, 48]). It is a p-type close-end coaxial High Purity germanium detector, with a crystal of  $190 \text{ cm}^3$  and a copper cryostat. It is operated inside a shield made of 10 cm of archaeological lead plus 15 cm of low activity lead, enclosed in a plastic bag continuously flushed with boil-off nitrogen to avoid radon intrusion. The electronic chain for the data acquisition is based on a linear amplifier<sup>19</sup> and an analog-to-digital converter<sup>20</sup>.

The detector background is periodically characterized by taking data with no sample for periods of time of at least one month; the total counting rate below 3 MeV is at the level of 5 c/h. Activities of different sub-series in the natural chains of  $^{238}\text{U}$ ,  $^{232}\text{Th}$  and  $^{235}\text{U}$  as well as of common primordial, cosmogenic or anthropogenic radionuclides like  $^{40}\text{K}$ ,  $^{60}\text{Co}$  and  $^{137}\text{Cs}$  are typically evaluated by analyzing the most intense gamma lines of different isotopes; upper limits are derived if the gross signal does not statistically differ from the background signal [49, 50]. The detection efficiency is determined by Monte Carlo simulations based on Geant4 [51] for each sample, accounting for intrinsic efficiency, the geometric factor and self-absorption of the sample. The simulation environment has been validated by comparing the measured efficiency curve with a  $^{152}\text{Eu}$  reference

source of known activity with the simulated one [48]; a conservative overall uncertainty of 30% is considered for the deduced efficiency and properly propagated to the final results.

A wide range of materials and components related to Micromegas readout planes and the whole set-up of TREX-DM has been taken into consideration, like the gas vessel, the field cage, the radiation shielding or the electronic acquisition system. Massive elements and those in contact with the sensitive volume of the detector are in principle the most relevant. In the following, the screened samples will be described and the results presented. The activity values obtained are summarized in Table 1; reported errors include both statistical and efficiency uncertainties.

### 4.1 Shielding and vessel

Lead and copper are commonly used to reduce the external gamma background in passive shieldings. Several metal samples from different suppliers were analyzed by GDMS and activities were obtained from the measured U, Th and K concentrations [48]. Lead samples from the Spanish company Mifer for two different raw materials were considered (#1-2 of Table 1)<sup>21</sup>.

Copper is also used for mechanical and electric components: vessel, central cathode, Micromegas readout planes, HV feedthroughs or rings in TREX-DM. Three copper samples with different origins were studied (#3-5 of Table 1). One is ETP (C11000) copper supplied by Sanmetal while the other two were made of OFE (C10100) copper<sup>22</sup> from Luvata, having different production mechanism (hot versus cold rolling). A Luvata copper sample with 681 g was screened with the germanium detector as well (#6 of table 1); the upper bounds on activities derived from this germanium spectrometry measurement were much less stringent than those from GDMS due to its limited sensitivity. Although the GDMS measurement of the Luvata copper has given information only on U and Th concentration, the upper limits derived are at the same level or even better than the germanium spectrometry results for the NOSV copper from the Norddeutsche Affinerie (re-branded as Aurubis) [52]. At TREX-DM, Luvata copper was used for the plates while the other copper components were made of ETP copper from Sanmetal.

<sup>19</sup>Canberra 2020.

<sup>20</sup>Canberra 8075.

<sup>21</sup>GDMS is not sensitive to the  $^{210}\text{Pb}$  content which is typically used to qualify bricks as low activity lead.

<sup>22</sup>Purity guaranteed at 99.99%.

**Table 1** Results obtained for the activity of the natural chains and some common radioactive isotopes in components and materials intended to be used at the TREX-DM setup. Values reported for  $^{238}\text{U}$  and  $^{232}\text{Th}$  correspond to the upper part of the chains and those of  $^{226}\text{Ra}$  and  $^{228}\text{Th}$  give activities of the lower parts. Reported errors correspond to  $1\sigma$  uncertainties and upper limits are given at 95% CL.

#	Material, Supplier	Technique	Unit	$^{238}\text{U}$	$^{226}\text{Ra}$	$^{232}\text{Th}$	$^{228}\text{Th}$	$^{235}\text{U}$	$^{40}\text{K}$	$^{60}\text{Co}$	$^{137}\text{Cs}$
1	Pb, Mifer	GDMS	mBq/kg	<1.2		<0.41			0.31		
2	Pb, Mifer	GDMS	mBq/kg	0.33		0.10			1.2		
3	Cu, Sammetal	GDMS	mBq/kg	<0.062		<0.020					
4	Cu, hot rolled, Luvata	GDMS	mBq/kg	<0.012		<0.0041			0.061		
5	Cu, cold rolled, Luvata	GDMS	mBq/kg	<0.012		<0.0041			0.091		
6	Cu, Luvata	Ge	mBq/kg		<7.4	<0.8	<4.3		<18	<0.8	<1.2
7	Kapton-Cu, LabCircuits	Ge	$\mu\text{Bq}/\text{cm}^2$	<160	<14	<12	<8	<2	<40	<2	<2
8	Teflon, Sammetal	Ge	mBq/kg	<157	<4.1	<6.6	<4.8	<4.8	<19	<1.2	<1.4
9	Teflon tube, RS	Ge	mBq/kg	<943	<21	<37	<31	<19	510 $\pm$ 170	<7.6	<8.0
10	Stycast, Henkel	Ge	mBq/kg	(3.7 $\pm$ 1.4)10 <sup>3</sup>	52 $\pm$ 10	44 $\pm$ 12	38 $\pm$ 9		(0.32 $\pm$ 0.11)10 <sup>3</sup>	<5.5	<6.5
11	Epoxy Hysol, Henkel	Ge	mBq/kg	<273	<16	<20	<16		<83	<4.2	<4.5
12	SMD resistor, Farnell	Ge	mBq/pc	2.3 $\pm$ 1.0	0.16 $\pm$ 0.03	0.30 $\pm$ 0.06	0.30 $\pm$ 0.05	<0.05	0.19 $\pm$ 0.08	<0.02	<0.03
13	SM5D resistor, Finechem	Ge	mBq/pc	0.4 $\pm$ 0.2	0.022 $\pm$ 0.007	<0.023	<0.016	0.012 $\pm$ 0.005	0.17 $\pm$ 0.07	<0.005	<0.005
14	CF40 flange, Pfeiffer	Ge	mBq/kg		14.3 $\pm$ 2.8	9.7 $\pm$ 2.3	16.2 $\pm$ 3.9	3.2 $\pm$ 1.1	<17	11.3 $\pm$ 2.7	<1.6
15	Connectors, Santec	Ge	mBq/pc	<77	9.2 $\pm$ 1.1	19.6 $\pm$ 3.6	18.5 $\pm$ 2.2	1.5 $\pm$ 0.4	12.2 $\pm$ 4.1	<0.6	<1.3
16	Connectors, Panasonic	Ge	mBq/pc	<42	6.0 $\pm$ 0.9	9.5 $\pm$ 1.7	9.4 $\pm$ 1.4	<0.95	4.1 $\pm$ 1.5	<0.2	<0.8
17	Connectors, Fujipoly	Ge	mBq/pc	<25	4.45 $\pm$ 0.65	1.15 $\pm$ 0.35	0.80 $\pm$ 0.19		7.3 $\pm$ 2.6	<0.1	<0.4
18	Flat cable, Somacis	Ge	mBq/pc	<370	101 $\pm$ 13	165 $\pm$ 29	164 $\pm$ 23		80 $\pm$ 25	<5	<15
19	Flat cable (rigid), Somacis	Ge	mBq/pc	<1.5 10 <sup>3</sup>	123 $\pm$ 17	225 $\pm$ 40	198 $\pm$ 29		112 $\pm$ 40	<5.8	<20
20	Flat cable (flexible), Somacis	Ge	mBq/pc	<102	<3.8	<4.0	<1.4	<1.8	<15	<0.7	<0.8
21	Flat cable, Somacis	Ge	mBq/pc	<45	<1.7	<1.8	<0.61	<0.77	<6.6	<0.3	<0.3
22	Flat cable, Somacis	Ge	mBq/pc	<14	0.44 $\pm$ 0.12	<0.33	<0.19	<0.19	1.8 $\pm$ 0.7	<0.09	<0.10
23	RG58 cable, Pro-Power	Ge	mBq/kg	(2.2 $\pm$ 0.9)10 <sup>3</sup>	(0.9 $\pm$ 0.1)10 <sup>3</sup>	40 $\pm$ 12	29 $\pm$ 8	<212	108 $\pm$ 43	<9.2	<8.9
24	Teflon cable, Druflon	Ge	mBq/kg	<104	<2.2	<3.7	<1.7	<1.4	21.6 $\pm$ 7.4	<0.7	<0.8
25	Teflon cable, Axon	Ge	mBq/kg	<650	<24	<15	<9.9	<7.9	163 $\pm$ 55	<4.3	<5.1
26	Kapton tape, Tesa	Ge	mBq/kg	<1.7 10 <sup>3</sup>	<34	<40	<22	<14	(0.46 $\pm$ 0.15)10 <sup>3</sup>	<10	<10
27	FR4 PCB, Somacis	Ge	Bq/kg	31 $\pm$ 11	15.3 $\pm$ 2.1	25.5 $\pm$ 4.4	22.5 $\pm$ 3.5		15.5 $\pm$ 4.7	<0.16	
28	PTFE circuit, LabCircuits	Ge	Bq/kg	<36	4.7 $\pm$ 0.6	5.0 $\pm$ 1.1	6.2 $\pm$ 0.9	<0.50	4.5 $\pm$ 1.5	<0.16	<0.54
29	Cuflon, Crane Polyflon	Ge	mBq/kg	<103	<3.7	<3.6	<1.4	<1.8	<13	<0.6	<0.7
30	Classical Micromegas, CAST	Ge	$\mu\text{Bq}/\text{cm}^2$	<40		4.6 $\pm$ 1.6		<6.2	<46	<3.1	
31	Microbulk Micromegas, CAST	Ge	$\mu\text{Bq}/\text{cm}^2$	26 $\pm$ 14		<9.3		<14	57 $\pm$ 25	<3.1	
32	Kapton-Cu foil, CERN	Ge	$\mu\text{Bq}/\text{cm}^2$	<11		<4.6		<3.1	<7.7	<1.6	
33	Cu-kapton-Cu foil, CERN	Ge	$\mu\text{Bq}/\text{cm}^2$	<11		<4.6		<3.1	<7.7	<1.6	
34	Vacrel, Saclay	Ge	$\mu\text{Bq}/\text{cm}^2$	<19	<0.61	<0.63	<0.72	<0.19	4.6 $\pm$ 1.9	<0.10	<0.14



## 4.2 Field cage

Materials and components to be used inside the vessel, mainly related to the field cage have been screened [48].

The monolayer PCB made of kapton and copper used at the field cage, supplied by LabCircuits, was screened finding good radiopurity (#7 of Table 1); a sample with a surface of 260.15 cm<sup>2</sup> was considered. A cylinder of teflon (945 g) supplied by Sanmetal was measured and an acceptable radiopurity was found since only upper limits were derived (#8 of Table 1). This material is very widely used, due to its physical, mechanical, dielectric and optical properties. All teflon components at TREX-DM are from this supplier.

A tube supplied by RS and used in the calibration system described above, to move radioactive sources in and out of the detector, was measured (#9 of Table 1). It was made of 1-mm-thick teflon and had a diameter of 1 cm; the mass of the sample was 91 g. The high level of <sup>40</sup>K quantified advised against its final use and other tubes are being analyzed.

The radiopurity of two types of adhesives to be used to glue kapton elements was analyzed. One was Stycast 2850 FT (a two component, thermally conductive epoxy encapsulant) used with the catalyst 24LV, both from Henkel. The other was Hysol RE2039 (an epoxy resin also from Henkel having exceptional resistance to impact and thermal shock) used together with the hardener HD3561. Massive samples of 551 g for Stycast and 245 g for Hysol were prepared following the provider specifications. Results are quoted in rows #10-11 of Table 1. High activities of the natural chains and <sup>40</sup>K were measured for the stycast sample, which prevents its use, while for the Hysol epoxy no contaminant could be quantified and therefore it has been used at TREX-DM. It is worth noting that soldering has been completely avoided inside the vessel.

Resistors are used in field cages, as in other electronic circuits. Surface Mount Device (SMD) resistors supplied by Farnell (50 pieces) and by Finechem (100 pieces) were screened (#12-13 of Table 1). Activity values obtained for Finechem resistors are much lower than for Farnell ones. For this reason, Finechem resistors were used at TREX-DM.

Radiopurity information for the CF40 flange in the vessel for pumping was also available. The screened piece, from Pfeiffer, was made of 304L stainless steel having a mass of 347 g. The activity from the radioactive chains and <sup>60</sup>Co was quantified (#14 of Table 1).

## 4.3 Electronics

First results of the screening of different components related to the acquisition system of TREX-DM (some connectors and circuits) were already presented in [48]. More components have been recently analyzed and results are detailed here.

Various types of connectors have been screened. Narrow pitch connectors for board-to-board from the Panasonic P5K series and other ones supplied by Samtec were initially considered [48] (#15-16 of Table 1). The number of pieces in the samples was 15 (0.67 g/pc) for Panasonic connectors and 10 (2.2 g/pc) for the Samtec ones. Both types show activities of several mBq/pc for isotopes in <sup>232</sup>Th and the lower part of <sup>238</sup>U chains and for <sup>40</sup>K, as found also in [53] for similar connectors. All of them are made of Liquid Crystal Polymer (LCP), thus the activity measured is attributed to this material. Since these levels are too high, this kind of connectors must be avoided or properly shielded. Five connectors made of silicone (Fujipoly Gold 8000 connectors type C, 1.14 g/pc) were also screened, having lower activity of <sup>226</sup>Ra and specially of <sup>232</sup>Th (#17 of Table 1); its use in TREX-DM is foreseen in the future.

Very radiopure, flexible, flat cables made of kapton and copper have been developed in collaboration with Somacis, performing a careful selection of the materials included. Three different designs of flat cables have been screened; their dimensions and masses are indicated in Table 2 together with the number of units screened in each case. In the first design, the cables consisted of a flexible band ended by two rigid boards and large activities were found at the screening of several units (#18 of Table 1); to investigate their origin, one of the cables was cut and the flexible band and the two rigid heads were separately screened. Only upper limits were set for the flexible part, while activities of the same order than for the whole cable were found for the rigid heads (#19-20 of Table 1) pointing to materials there to be the main source of radioactive contamination. The specific activities quantified for these cables are at the level of 10 Bq/kg, typical of glass fiber; it seems that the glass fiber-reinforced materials at base plates of circuit boards can be a source of radioactive contamination [54]. Two cables produced with a second design as totally flexible cables were screened (#21 of Table 1), finding results compatible with those obtained for the flexible band of the first design (upper limits are about a factor of 2 lower because two units were analyzed for the new design). This measurement was useful to fix the allowed materials and procedures in the cables manufacture. The screening of the final design to be used in TREX-DM was performed for 12 units and activities of <sup>40</sup>K and <sup>226</sup>Ra were quantified, while upper limits were set for the other common radioisotopes (#22 of Table 1). The results are comparable with previous measurements and the inclusion in the sample of a larger number of cable units, being in addition more massive, has allowed to quantify some isotopes and to reduce the upper limits for the rest of nuclides. As the fabrication technique used for flat cables can be adapted to build a bulk Micromegas readout, the good results obtained make possible the use of these materials and technique also for the production of radiopure Micromegas readout planes.

Several kinds of high voltage and signal cables have been analyzed. A sample of coaxial cable RG58BU with jacket made of black PVC from Pro-Power was screened;

**Table 2** Main features of the samples of flat cables made of kapton and copper by Somacis and screened by germanium spectrometry to analyze and improve their radiopurity. Dimensions and masses given correspond to one cable unit.

Design	Units	Length (cm)	Width (cm)	Thickness (mm)	Mass (g)
First	8				33.2
Heads	1	3.3	6	1.65	14.0
Band	1	50.5	5	~0.4	19.6
Second	2	57.5	5-6	~0.4	24.7
Final	12	57.6	6.4	~0.7	54.6

it was 20-m-long having a mass of 723.4 g. Large activities were found for most of the radioisotopes (#23 of Table 1). A sample of the cable AWG 18/19/30  $\times$  10.0 CR from Druflon Electronics was also measured (#24 of table 1). It has Silver Plated Copper wires (19 wires, diameter of 0.225 mm each) with a teflon jacket with outer diameter of 0.25 inches; the sample was 10.65-m-long with a mass of 780.4 g. This Druflon cable is used to connect the field cage last ring to HV feedthrough. A sample of the coaxial low noise cable SML 50 SCA from Axon Cable S.A.S. was screened too (#25 of Table 1). The conductor is made of Silver Plated Copper Alloy, the dielectric of extruded PTFE, the screen of Silver Plated Copper and the outer sheath of taped PTFE. The length and mass of the sample were 43.76 m and 125.4 g and the cable has 1.1 mm as maximum diameter. The Axon cable is used to extract the mesh signal from the vessel. Only  $^{40}\text{K}$  activity was quantified for these two cables made basically of copper and teflon. Although the values of the activity per mass are lower for the Druflon cable, the Axon cable has a better radiopurity per unit length.

Finally, the kapton tape (Tesa 52408-00008-00) used throughout the set-up was screened. It is reported to have a polyimide backing with a silicone adhesive. The sample, with a mass of 49.1 g, was 33-m-long, 19-mm-wide and 65- $\mu\text{m}$ -thick; only  $^{40}\text{K}$  activity was quantified (#26 of Table 1).

#### 4.4 Micromegas readout planes

Different materials can be taken into consideration for PCBs. A 187.4-g sample of the PCB at the Micromegas produced by Somacis and used for the moment in TREX-DM was screened; it is made of FR4/phenolic for core and pre-preg together with copper and resin. Very large specific activities were found for the common radioisotopes (#27 of Table 1); as mentioned before, this was expected for glass-fiber reinforced materials [54]. In addition, FR4 should be disregarded not only because of high radioactivity, but also for an unacceptable high rate of outgassing. Kapton (or cirlex) and PTFE are in principle radiopure, as shown in the screening of the PCB made of kapton and copper supplied by LabCircuits and used at the field cage (#7 of Table 1). However, a 49-g circuit made of ceramic-

filled PTFE composite also from LabCircuits (#28 of Table 1) presented very high activities for the natural chains and  $^{40}\text{K}$ , precluding its use. Good radiopurity was found for cuflon samples from Crane Polyflon; a sample taken from a 1.57-mm-thick panel, made of PTFE sandwiched by two 35  $\mu\text{m}$ -thick copper sheets, and with a mass of 705.9 g was screened, setting upper limits for all the common isotopes (#29 of Table 1). However, the use of cuflon for Micromegas has been disregarded due to the difficulty to fix the mesh and also because bonding films to prepare multilayer PCBs have been shown to have unacceptable activity [53].

The radiopurity of Micromegas readout planes was first analyzed in depth in [25]. Main results obtained in this work are reproduced here for the sake of completeness. On the one hand, two samples (#30-31 of Table 1) were part of fully functional microbulk Micromegas readouts: a full microbulk readout plane formerly used in the CAST experiment and a classical Micromegas structure without mesh. Both of them had a diameter of 11 cm. The second sample represents an earlier stage in the manufacturing process than the full microbulk structure of the first sample, in which chemical baths have been applied to etch the kapton pillars and the mesh structure. On the other hand, two more samples (#32-33 of Table 1) were screened corresponding just to the raw foils used in the fabrication of microbulk readouts, consisting of kapton metalized with copper on one or both sides. Several circular wafers of the same diameter as the real detectors (11 cm) were considered in this case. The raw materials (kapton and copper, mainly) were confirmed to be very radiopure, since no contamination was quantified. Altogether, the obtained results proved that Micromegas readouts of the microbulk type are manufactured with radiopurity levels comparable to the cleanest detector components in low background experiments.

A new activity measurement for the Cu-kapton-Cu foil was carried out profiting the great capabilities of the BiPo detector [55] operating at the LSC. It is a large planar detector developed to measure mainly the SuperNEMO double beta source foils with sensitivity to few  $\mu\text{Bq/kg}$  of  $^{208}\text{Tl}$  and  $^{214}\text{Bi}$  (two isotopes produced in the decays of the natural chains of  $^{232}\text{Th}$  and  $^{238}\text{U}$ ), thus surpassing by almost two orders of magnitude the sensitivity of standard gamma spectroscopy. Preliminary results [56] have shown that the activities of both isotopes in the Cu-kapton-Cu foil are near the detector's sensitivity, i.e.,  $\sim 0.1 \mu\text{Bq/cm}^2$ .

Vacrel is a material used in the construction of bulk Micromegas and included in the Micromegas produced by Somacis for TREX-DM. A sample of vacrel sheets with a total surface of 4800  $\text{cm}^2$  and a mass of 65 g from Saclay was screened (#34 of Table 1); only  $^{40}\text{K}$  was quantified and upper limits were set for all the other common radioisotopes.

## 5 Background model of TREX-DM at LSC

As a required element to estimate the sensitivity of TREX-DM to low-mass WIMPs, we have created a first background model of the experiment, as it were installed and in operation at the LSC. This model is based on the screening program of all materials used in the setup (described in Sec. 4) and the simulation of the detector response. The section has been divided in four parts: the main contributions to the background model are detailed in Sec. 5.1; in Sec. 5.2, the simulation of the detector's response is described, as well as a crosscheck with real data; an analysis based on cluster features is then proposed and a first estimation of background levels is made in Sec. 5.3; finally, in Sec. 5.4, we extend former analysis to an electron/neutron discrimination based on a neutron source.

We have considered two light gas mixtures at 10 bar: Ar+2%iC<sub>4</sub>H<sub>10</sub> and Ne+2%iC<sub>4</sub>H<sub>10</sub>, which are good candidates to detect WIMPs of masses below 20 GeV and give a total active mass of 0.300 and 0.160 kg respectively. The background levels quoted in the following are referred to an energy window of reference of 2-7 keV, as it is low enough to avoid the contribution of most of K-fluorescence lines of the surrounding materials. Nevertheless, the final analysis of TREX-DM should consider a larger RoI and describe in detail its background spectrum, as in other Dark Matter experiments [57].

### 5.1 Main contributions to background model

For the most relevant setup components, we have simulated the radioactive isotopes and we have scaled the results by the measured activities described in Sec. 4. In some cases, we have considered a radiopure alternative, as it is planned for the near-future, like in the case of the Micromegas readout planes. For this component, we have imposed a secular equilibrium of both <sup>232</sup>Th and <sup>238</sup>U chains to estimate the activities of the different isotopes from those of <sup>208</sup>Tl and <sup>214</sup>Bi. In the case of teflon, we have used the activities reported by EXO-200, as the values in Table 1 (#8 and #9) are just upper limits. Finally, for the specific case of argon-based mixtures, we have considered the isotope <sup>39</sup>Ar, using the activity measured by DarkSide collaboration. The components and the activities included in this first background model of TREX-DM are detailed in Table 3.

We have not simulated some inner components like the cabling, the calibration tube and the copper and lead pieces used to shield the connectors. Their activities are in almost all cases below the sensitivity limit of germanium detectors, and can be considered negligible when compared to other components. Regarding external components of background, we have not included neither the interface cards and the AFTER-based electronics, nor the shielding, the environmental gamma flux and neutrons (from radioactivity and muon-induced in the shielding or in the rock [61]). Both electronics (mainly based on FR4 PCB,

**Table 3** Activities considered in the simulation for the different components of the TREX-DM experiment. Upper limits are given at 90% C.L.

Component	Isotope	Activity	Ref.
Muon flux	-	$5 \times 10^{-3} \text{ s}^{-1} \text{ m}^{-2}$	[58]
Copper vessel & cathode	<sup>232</sup> Th	< 4 $\mu\text{Bq/kg}$	This work
	<sup>238</sup> U	< 12 $\mu\text{Bq/kg}$	
	<sup>40</sup> K	< 61 $\mu\text{Bq/kg}$	
Connector	<sup>232</sup> Th	1.2 mBq/pc	This work
	<sup>238</sup> U	< 25 mBq/pc	
	<sup>40</sup> K	7.3 mBq/pc	
	<sup>60</sup> Co	< 0.1 mBq/pc	
Teflon field cage	<sup>232</sup> Th	< 1.2 $\mu\text{Bq/kg}$	[59]
	<sup>238</sup> U	< 9.7 $\mu\text{Bq/kg}$	
	<sup>40</sup> K	< 10.0 $\mu\text{Bq/kg}$	
Readout plane	<sup>232</sup> Th	< 120 nBq/cm <sup>2</sup>	[56]
	<sup>238</sup> U	110 nBq/cm <sup>2</sup>	
Target	<sup>39</sup> Ar	0.73 mBq/kg	[60]

#27 of Table 1) and environmental components are quite important and their contribution should be highly suppressed by a good shielding.

### 5.2 Simulation of the detector response

The simulation of the detector response can be divided into two blocks. The first one covers all the physical processes involved in the passage of gamma-rays and charged particles through matter, and is mainly based on Geant4 [51]. This code is widely used in astroparticle and high energy experiments, and has been validated in a wide range of detection techniques and experimental conditions. An accurate model of the detector and inner shielding has been created, as shown in Fig. 12. Version Geant4.10.0 and its corresponding data libraries have been used for all the simulations presented here. Physical processes and models commonly used in the context of underground experiments have been implemented for interactions of alpha, beta and gamma particles. In the case of muons, we have only considered electromagnetic processes, while for neutron-induced recoils, we have used the NeutronHP model. To accelerate the simulation, we have used the Decay0 code [62] as generator of initial events, instead of the Geant4 Radioactive Decay Module. Decay0 generates the particles from the decay of radioactive nuclides of many known unstable isotopes.

The second block simulates all physical processes of a TPC: the generation of electrons in the gas, the diffusion effects during the drift to the readout plane, the charge amplification at the Micromegas readout and the generation of signals both at mesh and strips. It is based on the REST program [63], with some minor changes due to the two-volumes geometry and the AFTER-based electronics. The resulting data has the same format as the DAQ data, so as both real and simulated data may be analyzed by

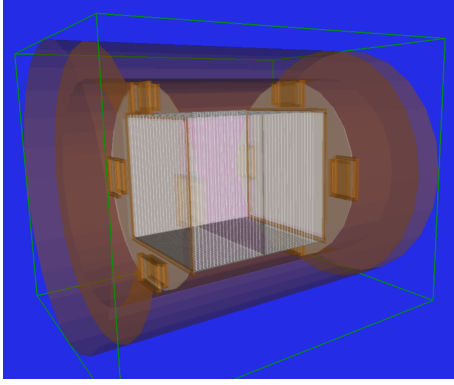


**Fig. 12** A view of the TREX-DM geometry implemented in Geant4. The cylindrical copper vessel (orange volumes) contains a circular base with four shielded boxes (dark gray surface with four yellow boxes), two active volumes (in light gray), the field cage and degrader (white walls) and a central cathode.

the same routines. We describe step by step the complete simulation chain:

- **Primary electrons:** The number of electrons ( $n_e$ ) generated by an energy deposit ( $E$ ) follows a distribution, which is empirically described by the average energy needed to produce an electron-ion pair ( $W$ ) and the Fano factor ( $F$ ). With these parameters:  $n_e = E/W$  and  $\sigma^2 = F \times n_e$ . For simplicity, we have combined the primary charge fluctuations with the amplification one in a later step. The values of  $W$  are detailed in Table 4.
- **Diffusion effects:** Each primary electron is projected to the XY plane and the time line following two gaussian distributions, whose widths are calculated by the distance to the readouts and the gas parameters (drift velocity, longitudinal and transversal diffusion coefficients) generated by Magboltz [64]. The gas parameters are detailed in Table 4.
- **Charge amplification:** The Micromegas readout amplifies the primary charge but it also introduces a fluctuation due to the avalanche formation. This variation depends on the gas and on the readout [45]. In this model, a charge amplification of  $10^3$  has been set, while avalanche fluctuations have been combined with the primary ones, and arbitrarily set to reproduce an energy resolution of 13% FWHM at 5.9 keV, which is the best value measured by a fully equipped Micromegas readout plane [27]. For simplicity, we have not considered any surface dependence of gain.
- **X-Y readout:** The detector readout is divided in pads, which are alternatively interconnected in X and Y directions. This specific feature is simulated dividing the amplified charge between X and Y planes by:  $Q_X = d_Y/(d_X + d_Y) \times Q$  and  $Q_Y = d_X/(d_X + d_Y) \times Q$ , where  $d_X$  and  $d_Y$  are respectively the minimum distance to pixels connected to X and Y directions.
- **Electronics response:** Each X and Y charge create a pulse, whose amplitude and widths are calculated con-

**Table 4** Summary of the gas parameters used in the simulation. Velocity and diffusion coefficients have been calculated using Magboltz [64] and considering a reduced drift field of 100 V/cm/bar and a gas pressure of 10 bar.

Gas	$W$ eV	Velocity cm/ $\mu$ s	Diffusion ( $\mu$ m cm $^{-0.5}$ )	
			Long.	Trans.
Ar+2% $i$ C $_4$ H $_{10}$	26.3	3.33	133.5	221.2
Ne+2% $i$ C $_4$ H $_{10}$	36.4	2.18	107.2	168.2

sidering the AFTER-based features [37, 38]: a sampling time of 10 ns, a shaping time of 100 ns and a transfer function of 10 mV/fC.

The expected signals in TREX-DM are nuclear recoils with energies below 20 keV. These events will create short tracks of a few microns length, which will then induce two compact group of active strips or *clusters* at both XZ and YZ directions. Their widths will be short and will be mainly defined by diffusion effects. Only at higher energies (or low gas pressures), the cluster features may be slightly different for electrons and neutrons due to the longer tracks of the former [65]. For this reason, we have applied the analysis used in CAST Micromegas detectors [21], to separate this type of events from complex topologies, that may be generated by high energy gammas or cosmic muons. We calculate first the cluster width in each direction by

$$\sigma_a = \sqrt{\frac{\sum_j q_j \times (a_j - \bar{a})^2}{\sum_j q_j}} \quad (1)$$

where  $a = X$  or  $Y$ ,  $q_j$  is the pulse integral and the index  $j$  runs over the set of event's pulses. From these two variables, two cluster observables are defined: the XY width,  $\sigma_{XY} = \sqrt{\sigma_X^2 + \sigma_Y^2}$ , which is mainly determined by the event topology and transversal diffusion; and the width balance,  $\Delta\sigma_{XY} = (\sigma_Y - \sigma_X)/(\sigma_X + \sigma_Y)$ , which only depends on energy as charge fluctuations between the two readout projections increase at low energy as less charge is shared. The last observable is the width in Z direction ( $\sigma_Z$ ), which is calculated using the pulses of both XZ and YZ planes as

$$\sigma_z = v_{drift} \times \sigma_t = v_{drift} \times \sqrt{\frac{\sum_j q_j \times (t_j - \bar{t})^2}{\sum_j q_j}} \quad (2)$$

where  $v_{drift}$  is the electron drift velocity,  $q_j$  is the pulse integral,  $t_j$  is the temporal position of the pulse maximum and the index  $j$  runs over the set of event's pulses. This observable includes information both on the intrinsic event's topology and the longitudinal diffusion.

These observables have been used to validate the complete simulation chain, by comparing their distributions to those of real data. This validation was initially made in [63] for the events acquired by a CAST Micromegas-based TPC when it was irradiated by a  $^{55}\text{Fe}$  source. We have repeated it for the TREX-DM detector irradiated by a  $^{109}\text{Cd}$  source (x-rays of 22.1 and 24.9 keV) situated at a



calibration point and the vessel filled of Ar+2%iC<sub>4</sub>H<sub>10</sub> at 2 bar. With this aim, a calibration tube of 1 mm-thickness has been implemented, but not the metallic source container. The comparison between the real and the simulated spectra is shown in Fig. 13. The positions of the x-ray lines of the source and the fluorescences generated by the readouts materials (iron and copper) match perfectly. However, the lines are not so well defined in real data, as the Micromegas readouts show a factor 2 worse energy resolution than the one simulated. This fact may be improved in the future with better readout planes and a more suitable gas mixture.

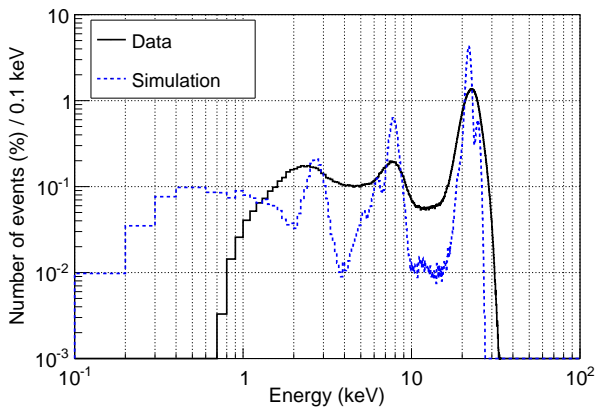


**Fig. 13** Comparison of the measured (black line) and simulated (dashed blue line) energy spectra generated by the strip signals when one of the active volumes is irradiated by a <sup>109</sup>Cd source situated at a calibration point. The vessel is filled with Ar+2%iC<sub>4</sub>H<sub>10</sub> at 2 bar. At both spectra, the K<sub>α</sub> (22.1 keV) and K<sub>β</sub> (24.9 keV) x-ray lines generated by the source are present, as well as their corresponding escape peaks, located at 19.1 and 21.9 keV. The argon, iron and copper K-fluorescences, respectively induced by the source at the argon gas, the Micromegas readout plane and the central cathode, are also present at 3.0, 6.4 and 8.0 keV.

The comparison of the observables (the cluster widths in XY-plane and Z-direction,  $\sigma_{XY}$  and  $\sigma_Z$ , and the width balance,  $\Delta\sigma_{XY}$ ) between real and simulated events is made in Fig. 14. The distributions match satisfactory and we reproduce its dependence with energy. This dependence is qualitatively understood by diffusion and other detector response effects. In general, it responds to the spatial distribution of the events in the conversion volume, as the range of primary electrons is too small compared to diffusion effects. Copper fluorescences (at 8.0 keV) are expected roughly everywhere in the detector, but with more intensity close to the cathode. In contrast, iron fluorescences (at 6.4 keV) are only emitted from the readouts, are absorbed near them due to their short mean free path and, in consequence, their clusters are narrow. The decrease of the XY-width ( $\sigma_{XY}$ ) at low energies is attributed to a threshold effect in the strip electronics, that effectively cuts the low energy tails of the electron clouds, an effect more evident in the real data than in the simulated one. Fi-

nally, the balance of cluster widths ( $\Delta\sigma_{XY}$ ) shows a wider distribution for low energy events, as the relative charge differences between each direction increase.

### 5.3 Analysis and results

Two analysis have been developed to perform event-by-event signal identification and background rejection using the topological information provided by the readout planes: one based on x-rays cluster features, which is described in this section, and another one based on a neutron source, described in Sec. 5.4. In principle, the second one is more adequate to our physic case, as the WIMP-induced recoil signal is similar to that of a neutron. However, as a calibration with a neutron source has not been possible yet, we found interesting to first create an analysis based on x-rays to make a comparison with real data.

The x-ray analysis is composed of two parts. In the first one, a veto area of 5 mm thickness at the borders of each readout plane is used to reject background events, with a small reduction of the signal efficiency (91.8%). This veto is specially useful in the case of cosmic muons, as less than 10% events are kept at the RoI. It is also powerful for events coming from the readout surface, as alphas or high energy electrons are easily rejected. In the rest of the cases, the rejection power of this selection cut is modest.

The second part of the analysis is based on the three observables defined in the previous section: the widths in XY ( $\sigma_{XY}$ ) and Z directions ( $\sigma_Z$ ), and the the width balance ( $\Delta\sigma_{XY}$ ). A calibration with a <sup>109</sup>Cd source is used to create the distribution histograms ( $P_i^j$ ) of each observable  $i$  for the two main x-ray lines  $j$ , situated at 3.0 and 22.1 keV. These lines, present both in argon- and neon-based mixtures as shown in Fig. 15, are generated by the radioactive source, with an extra contribution of the escape peak in the case of argon. To have access to the 3.0 keV line, the plastic calibration tube has been removed. We have discarded the use of the iron (at 6.4 keV) and copper K-fluorescences (at 8.0 keV), as they may be mainly absorbed at the edges of the fiducial volumes and may make the analysis dependent on the z-position. Note that most of the copper fluorescences come from the central cathode and their events will show larger widths than those of the <sup>109</sup>Cd x-ray lines, as their corresponding electrons must drift along all the fiducial volume. Meanwhile, iron fluorescences are induced at the Micromegas readout and their events will show narrower widths because of their shorter drift distance.

The distribution histograms, shown in Fig. 16, are used to define two likelihood ratios  $\mathcal{F}^j$  of the form

$$\mathcal{F}^j = -\log \mathcal{L}^j = -\sum_{i=1}^3 \log \left( \frac{P_i^j}{1 - P_i^j} \right) \quad (3)$$

which will then be applied to the data-sets from the different radioactive isotopes and components to select signal-like events in two different energy ranges: the 3 keV x-ray

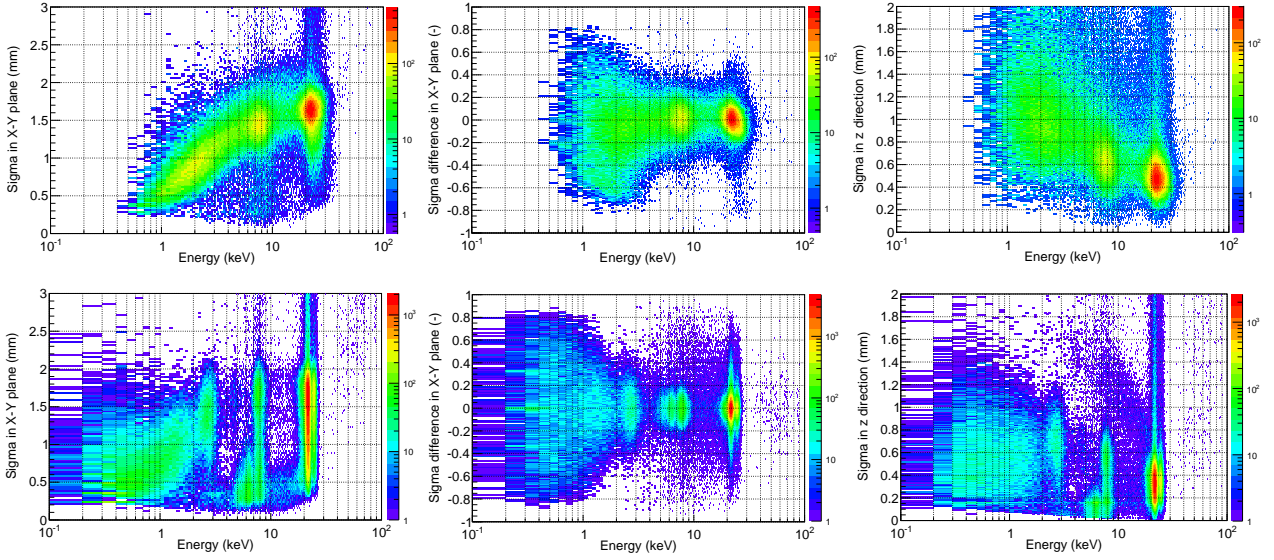


**Fig. 14** Comparison between the analysis observables (left: the  $XY$  width,  $\sigma_{XY}$ ; center: the balance of cluster widths,  $\Delta\sigma_{XY}$ ; right: the  $Z$  width,  $\sigma_Z$ ) for real (top) and simulated events (bottom) generated by a  $^{109}\text{Cd}$  source situated at a calibration point of TREX-DM, when it was filled with  $\text{Ar}+2\%\text{iC}_4\text{H}_{10}$  at 2 bar.

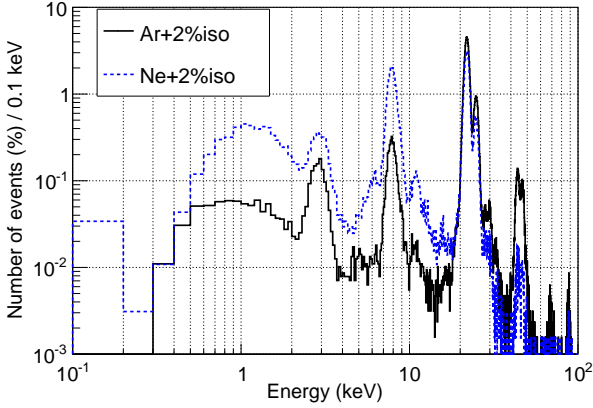


**Fig. 15** Simulated energy spectra generated by a  $^{109}\text{Cd}$  source situated at a calibration point of TREX-DM, when it is filled with  $\text{Ar}+2\%\text{iC}_4\text{H}_{10}$  (black line) and  $\text{Ne}+2\%\text{iC}_4\text{H}_{10}$  (dashed blue line) at 10 bar. The main peaks are generated by the  $K_\alpha$  (22.1 keV) and  $K_\beta$  (24.9 keV) x-ray lines of the source. The iron and copper K-fluorescences, induced by the source at the Micromegas readout plane and the central cathode, are also present at 6.4 and 8.0 keV, respectively. At 3.0 keV there is an intense peak which includes both the  $L_\alpha$  (at 2.98 keV) and the  $L_\beta$  (at 3.15 keV) x-ray lines of the  $^{109}\text{Cd}$  source, and the argon K-fluorescence (at 2.96 keV) in the case of the argon-isobutane mixture.

line is used for energies up to 10 keV, while the 22.1 keV is used from 10 to 100 keV. An analysis efficiency of 90% is set, which defines an upper acceptance limit  $q^j(90\%)$  for each function  $\mathcal{F}^j$ . These values are detailed for each gas mixture in Table 5. The total signal efficiency, which results of the combination of the veto- and the cluster-

**Table 5** Summary of the cluster-based analysis parameters: x-ray lines, selection and application energy ranges and upper acceptance limits in argon- and neon-isobutane mixtures.

Line (keV)	Energy range (keV)		Upper limit	
	Selection	Application	Argon	Neon
3.0	2.0-4.0	0.0-10.0	13.25	13.75
22.1	21.0-23.0	10.0-100.0	11.75	11.05

based analysis efficiencies, is 82.6%. The rejection factor<sup>23</sup> varies from  $\sim 18$  for muon-induced events down to  $\sim 2.5$  for events generated at the readout surface, and  $\sim 1.5$  for vessel activities.

The resulting background spectra for the argon- and neon-isobutane are shown in Fig. 17. Each background spectrum has a flat and continuous component in a wide range of energies, generated by gamma events that have suffered a Compton process. This flat spectrum decays at high energy due to an efficiency loss. At low energies, clusters show a shorter  $XY$ -width and a larger  $Z$ -width in comparison to 3 keV x-rays clusters (see Fig. 16), which causes a signal loss. These differences are due to the energy dependences discussed in Sec. 5.2. Apart from that, there are two intense peaks at 6.4 and 8.0 keV, which respectively correspond to the iron and copper K-fluorescences. These events are induced at the Micromegas readout plane and the central cathode by gammas. Finally, the contributions of the cathode, the Micromegas readout and the field cage show other lines between 10 and 20 keV, mainly generated by the x-ray lines of  $^{228}\text{Ac}$  (at energies of 13.0, 16.2 and 19.0 keV),  $^{212}\text{Bi}$  (at 14.6 keV) and  $^{214}\text{Pb}$  (at 12.9 keV).

<sup>23</sup>Defined as the ratio of events in the RoI before and after the application of the selection criteria.

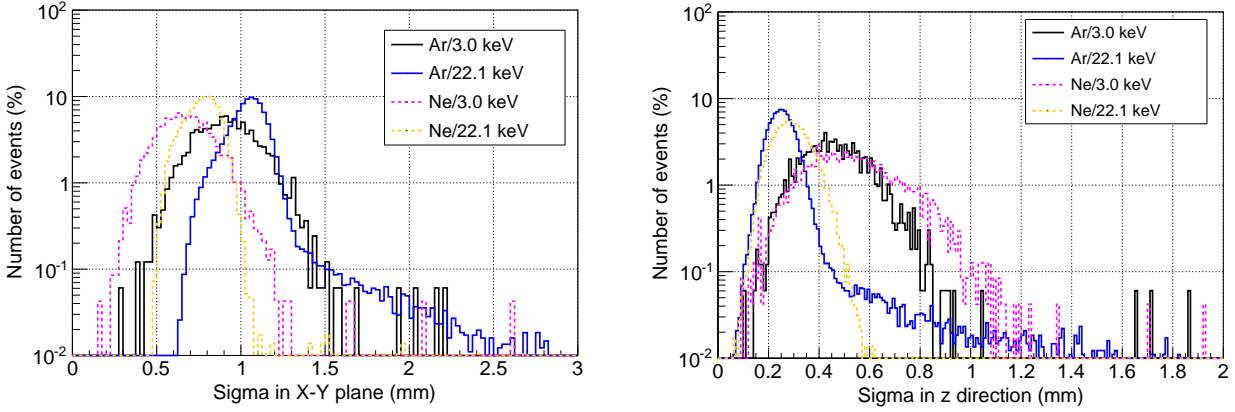


**Fig. 16** Distribution histograms of the  $XY$  width (left) and  $Z$  width (right) for the x-ray events at 3.0 and 22.1 keV generated by the  $^{109}\text{Cd}$  source situated at a calibration point of TREX-DM, when it is filled with  $\text{Ar}+2\%\text{iC}_4\text{H}_{10}$  (black and blue lines) and  $\text{Ne}+2\%\text{iC}_4\text{H}_{10}$  (dashed magenta and orange lines) at 10 bar.

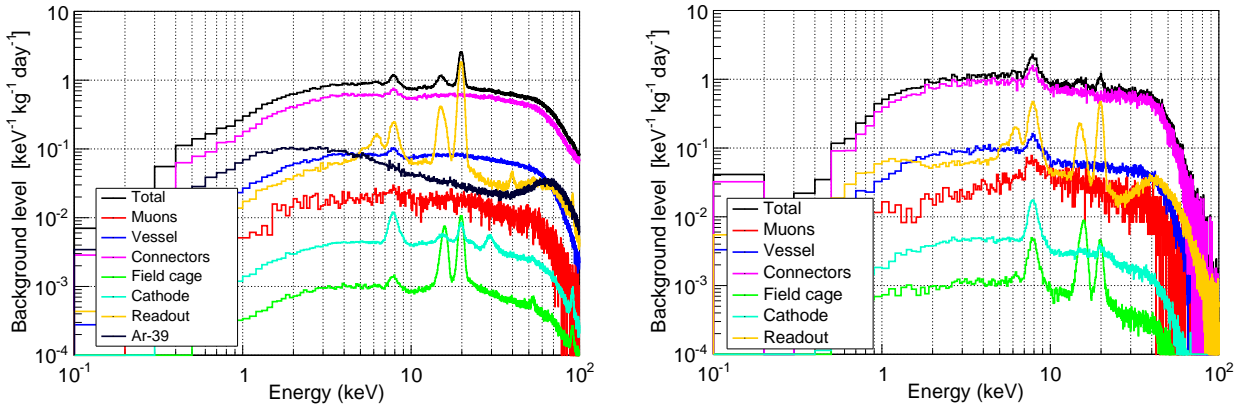


**Fig. 17** Background spectrum expected in TREX-DM experiment (black line) during a physics run at LSC if operated in  $\text{Ar}+2\%\text{iC}_4\text{H}_{10}$  (left) or  $\text{Ne}+2\%\text{iC}_4\text{H}_{10}$  at 10 bar. The contribution of the different simulated components is also plotted: external muon flux (red line), vessel contamination (blue line), connectors (magenta line), field cage (green line), central cathode (cyan line), Micromegas readout planes (orange line) and  $^{39}\text{Ar}$  isotope for the argon case (dark blue line).

The background level in the RoI (2-7 keV) and its different contributions are detailed in Table 6. For the argon-(neon-) isobutane mixture, the total background level is 0.85 (1.12) counts  $\text{keV}^{-1} \text{kg}^{-1} \text{day}^{-1}$ . For both gases, the main contribution (68% and 82% of background events, respectively) is due to the connectors, followed by the Micromegas readout planes (10% and 8%) and the vessel (9% and 8%). In the case of argon, the contribution by the  $^{39}\text{Ar}$  isotope is similar to the readout and vessel ones. We must also note that both the vessel and Micromegas contributions are just upper limits set by radiopurity measurements. In summary, we can conclude that a background level of  $\sim 1$  count  $\text{keV}^{-1} \text{kg}^{-1} \text{day}^{-1}$  is feasible if the final configuration of TREX-DM experiment follows these conclusions:

- **Gas:** in the case of argon, it should be extracted from underground sources because an atmospheric one may increase the  $^{39}\text{Ar}$  contribution a factor  $10^3$ . There are

prospects to further reduce this contribution, as recently shown in [60].

- **Connectors:** they must be shielded with a 1 cm-thick layer of copper and a 1 cm-thick layer of lead. To reach lower values, they should be put further away from the active volumes, behind the copper basements or, in the best case, out of the vessel.
- **Readout planes:** they should be made of copper and kapton, using either a radiopure version of the bulk technology or the microbulk one. Note that the activity of the actual readouts (defined by FR4 PCB, #27 of Table 1) is  $10^4$  higher than the required one.
- **Outer shielding:** it should be designed to reduce the contribution of the external gamma flux and neutrons to these levels. We must note that even if the electromagnetic muon processes do not give an important contribution to background, muon-induced neutrons in the external shielding or in the rock must be included in the final background model [61].

**Table 6** Estimated background levels (in  $\text{keV}^{-1} \text{kg}^{-1} \text{day}^{-1}$ ) of TREX-DM in the RoI (2-7 keV) for an argon- and neon-isobutane mixture at 10 bar. Values have a statistical error less than 5% and their error is mainly dominated by the measurement error of the component's activity.

Component	Material	Argon	Neon
Muon flux		0.019	0.029
Vessel	Copper	< 0.079	< 0.093
Connectors	Fujipoly	0.58	0.90
Field cage	Teflon	0.00096	0.0012
Cathode	Copper	< 0.0042	< 0.0046
Readout planes	Cu-Ka-Cu	< 0.086	< 0.095
Target	$^{39}\text{Ar}/-$	0.084	-
Total		0.85	1.12

#### 5.4 An electron/neutron discrimination analysis

The analysis presented in Sec. 5.3 is based on a x-ray  $^{109}\text{Cd}$  source, as WIMP induced nuclear recoils and low energy x-rays will show similar features at high gas pressures. As the mean free path of these x-rays is quite short and the source is situated at the cathode, the main part of these x-rays may be absorbed in the first few cm near this element. Their corresponding cluster features may be different than those absorbed near the readouts, which could create an artificial fiducial cut along the z-axis. Neutrons do not show this behavior as their mean free path is much longer than the detector's dimensions, and all its events would be uniformly generated at the fiducial volumes. Apart from that, we could not discard that even at high pressures, nuclear recoils may show narrower clusters than x-rays' ones, further reducing the estimated background level. As shown in [65], this background reduction is a factor  $10^3$  at 10-20 keV range in  $\text{CF}_4$  at 50 mbar.

For all these reasons, we have simulated a  $^{252}\text{Cf}$  neutron source, situated at a calibration point of TREX-DM, using the energy distribution measured in [66] and taking into account the gas quenching factor. The resulting energy spectra have a decay form both in Ar+ and Ne+2% $\text{iC}_4\text{H}_{10}$  at 10 bar, as shown in Fig. 18. Even if no peak is present, we have chosen two energy ranges at 3.0 and 22.0 keV to generate the distribution histograms of the observables. These values are far from the K-fluorescences of the surrounding materials to avoid any position dependence of the selected events. As an example, the distributions of the XY- and Z-widths are shown in Fig. 19. Comparing these distributions with those of Fig. 16, we note that nuclear recoils clusters show narrower widths in both directions. For instance, the distributions of the 22.1 keV line respectively peak at 1.1 and 0.25 mm for  $\sigma_{XY}$  and  $\sigma_Z$ , while these values are 0.8 and 0.15 mm in the case of nuclear recoils of 22.0 keV. However, their distributions cannot be totally separated from the x-rays' one and the expected rejection factor is modest.

Once the distribution histograms ( $P_i^j$ ) have been generated, we have defined two likelihood ratios using the Eq. 3. We have then set an analysis efficiency of 90%,

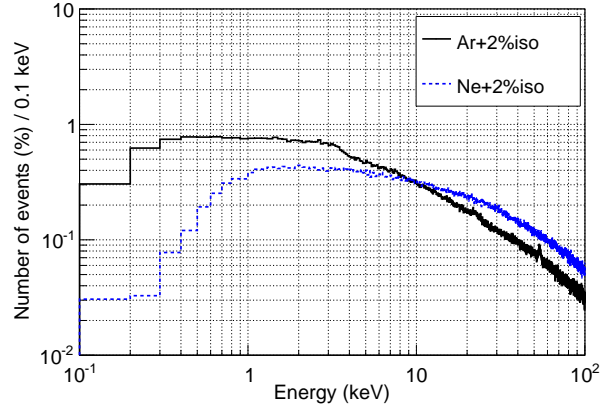


**Fig. 18** Simulated energy spectra generated by a  $^{252}\text{Cf}$  neutron source situated at a calibration point of TREX-DM, when it is filled with Ar+2% $\text{iC}_4\text{H}_{10}$  (black line) and Ne+2% $\text{iC}_4\text{H}_{10}$  (dashed blue line) at 10 bar.

**Table 7** Summary of the electron/neutron analysis parameters: likelihood ratios, selection and application energy ranges and upper acceptance limits in argon- and neon-isobutane mixtures.

Likelihood ratio	Energy range (keV)		Upper limit	
	Selection	Application	Argon	Neon
1	2.0-4.0	0.0-10.0	12.75	12.45
2	21.0-23.0	10.0-100.0	13.05	12.45

which has fixed an upper acceptance limit  $q^j$  (90%) for each function. These values are detailed for each gas mixture in Table 7. For simplicity, we have kept the same application energy ranges as in the previous section and the same fiducial volumes (total signal efficiency of 82.6%). The rejection factors are higher in general ( $\sim 30$  for muon-induced events and  $\sim 2.5$  for vessel events), except for the surface contaminations of the readout planes, as it is slightly worse ( $\sim 2.1$  instead of  $\sim 2.5$ ).

The resulting background spectrum (shown in Fig. 20 for Ar+2% $\text{iC}_4\text{H}_{10}$  at 10 bar) is similar in shape as that obtained in x-ray analysis. The flat spectrum range to sub-keV energies (down to 0.5 keV). This fact can be explained by a higher signal efficiency for this analysis at low energies, as cluster features are more similar to those of the 3 keV line in the case of the  $^{252}\text{Cf}$  source.

The background level in the RoI (2-7 keV) and its different contributions are detailed in Table 8. For the argon- (neon-) isobutane mixture, the total background level is 0.64 (0.86) counts  $\text{keV}^{-1} \text{kg}^{-1} \text{day}^{-1}$ . These total values are respectively  $\sim 25\%$  lower in argon- and  $\sim 23\%$  in neon-isobutane at 10 bar than those shown in Table 6. This reduction is more intense for some contributions like the vessel (respectively 41% and 43%), while there is an increase in others like the Micromegas readouts' one (22% and 53%). This result confirms that electron and nuclear recoils are not distinguishable in these gases at high pressures. However, an analysis based on the point-like cluster



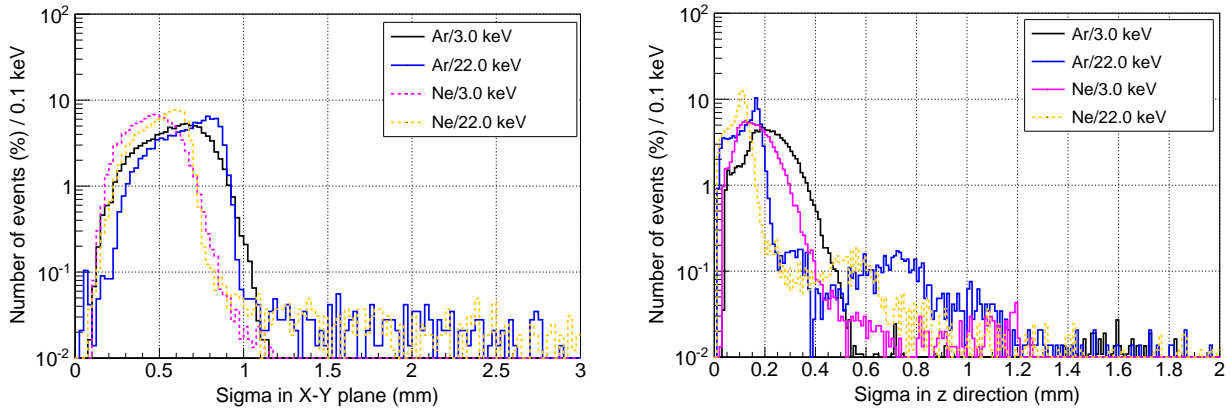


**Fig. 19** Distribution histograms of the XY width (left) and Z width (right) for the neutron events at 3.0 and 22.0 keV generated by a  $^{252}\text{Cf}$  neutron source situated at a calibration point of TREX-DM, when it is filled with Ar+2% $i\text{C}_4\text{H}_{10}$  (black and blue lines) and Ne+2% $i\text{C}_4\text{H}_{10}$  (dashed magenta and orange lines) at 10 bar.

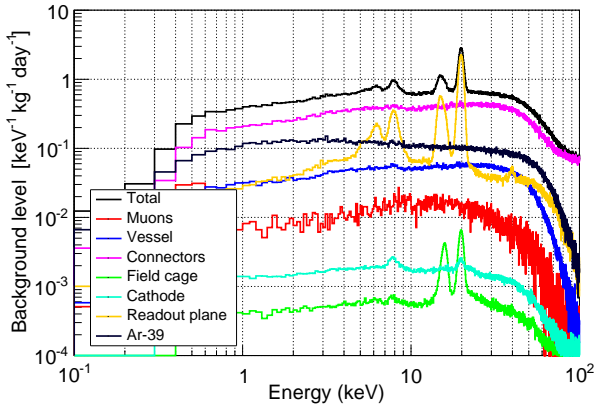


**Fig. 20** Background spectrum expected in TREX-DM (black line) during a physics run at LSC if operated in Ar+2% $i\text{C}_4\text{H}_{10}$  at 10 bar using an electron/neutron discrimination analysis. The contribution of the different components is also plotted: external muon flux (red line), vessel contamination (blue line), connectors (magenta line), field cage (green line), central cathode (cyan line), Micromegas readout planes (orange line) and  $^{39}\text{Ar}$  isotope (dark blue line).

features (be it x-rays or nuclear recoils) is able to discriminate more complex background events and provides a rejection factor of about 18-30 for muon-induced events, 1.5-2.5 for vessel activities and 2.1-2.5 for surface contaminations of the readout planes.

## 6 Sensitivity to low-mass WIMPs

TREX-DM could be sensitive to a relevant fraction of the low-mass WIMP parameter space. Figure 21 shows the 90% C.L. projected sensitivity of TREX-DM assuming an energy threshold of 0.4 keVee and a total exposure of 1 kg $\times$ y in argon and neon, under conservative and realistic values of a flat-shaped background level: 100 and 1 keV $^{-1}$  kg $^{-1}$  day $^{-1}$ , respectively.

**Table 8** Estimated background levels (in keV $^{-1}$  kg $^{-1}$  day $^{-1}$ ) of TREX-DM in the RoI (2-7 keV) for an argon- and neon-isobutane mixture at 10 bar, using an analysis based on  $^{252}\text{Cf}$  neutrons. Values have a statistical error less than 5% and its error is mainly dominated by the measurement error of the component's activity.

Component	Material	Argon	Neon
Muon flux		0.011	0.029
Vessel	Copper	< 0.043	< 0.064
Connectors	Fujipoly	0.32	0.64
Field cage	Teflon	0.0005	0.0008
Cathode	Copper	< 0.0016	< 0.0024
Readout planes	Cu-Ka	< 0.10	< 0.146
Target	$^{39}\text{Ar}/-$	0.13	-
Total		0.60	0.89

The projected exclusion curves have been derived using a binned Poisson method [14] with background suppression and energy binning of 100 eVee. This simple method works relatively well in case of large background levels, like ours. The Poissonian probability  $p$  of observing  $N$  or more events, where  $N = s + b$ , being  $s$  and  $b$  the signal and background events, is  $p = \sum_{k=s+b}^{\infty} \frac{e^{-b} b^k}{k!}$ , from which we can derive an exclusion contour at  $1 - \alpha$  confidence level by looping on the scattering cross-section  $\sigma_N$ , for each WIMP mass, until  $p < \alpha$ , being  $\alpha$  set at 0.1. As the quenching factor of neither gaseous argon nor neon has been measured yet, we have considered a conservative value of 0.157, corresponding to germanium at 1 keVnr [67]. This value is lower than those derived from Lindhard model [68] and the value of  $\sim 0.3$  measured for scintillation light in liquid argon in [69]. The other input parameters we have used include the standard WIMP halo model with Maxwellian velocity distribution, conventional astrophysical parameters as well as a WIMP coupling to neutrons equal to coupling to protons.

It is shown that under these hypotheses the experiment could reach higher sensitivity to low-mass WIMPs ( $m_\chi <$

8 GeV) than many of the current experiments, and could exclude the “region of interest” invoked by some positive interpretations of some Dark Matter experiments.

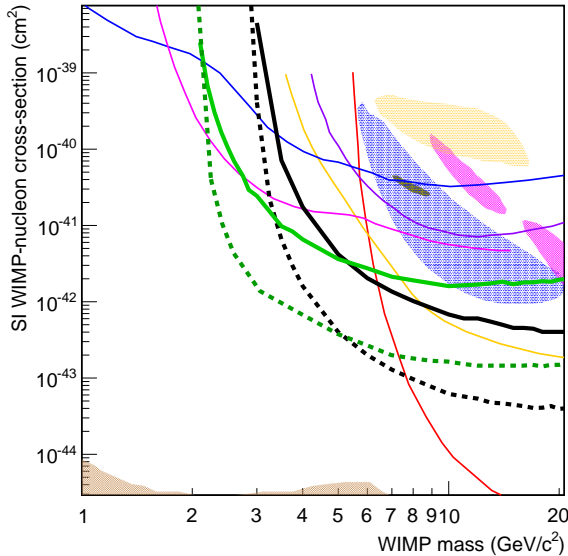


**Fig. 21** 90% confidence level projected sensitivity of TREX-DM assuming an energy threshold of 0.4 keVee and a total exposure of 1 kg×yr in argon (black thick lines) and neon (green thick lines) with a conservative (solid) and realistic (dotted) assumptions on the background levels of 100 and 1 keV<sup>-1</sup>kg<sup>-1</sup>d<sup>-1</sup>, respectively. Closed contours shown are CDMS II Si [70] (blue, 90% C.L.), CoGeNT [11] (dark gray, 90% C.L.), CRESST-II [12] (magenta, 95% C.L.), and DAMA/LIBRA [10, 14] (orange, 90% C.L.). For comparison we also show 90% C.L. exclusion limits from SuperCDMS [7] (orange), CDMSlite [18] (magenta), LUX [3] (red), CDEX [17] (purple) and CRESST-II 2015 [71] (blue).

## 7 Conclusions

New detection techniques, focused on the use of light target nuclei together with low energy thresholds, are needed to explore the low-mass range of the WIMP parameter space. Recent advances in radiopure Micromegas readout planes for gaseous TPCs and in electronics are improving the low-background prospects and scalability of Micromegas-based TPCs. If we add to these features the tracking capabilities and the low intrinsic energy threshold, they are a good detection option for the search of low-mass WIMPs. In this context, we present TREX-DM, a prototype built to test this concept. It is designed to host an active detection mass of  $\sim 0.300$  kg of Ar at 10 bar, or alternatively  $\sim 0.160$  kg of Ne at 10 bar, with an energy threshold below 0.4 keVee, and is fully built with radiopure materials.

The experiment consists of a copper vessel divided into two active volumes, each of them equipped with a

field cage and a bulk Micromegas readout plane. Signals are extracted from the vessel by flat cables and are read by an AFTER-based electronics. Each side is calibrated at four different points by a <sup>109</sup>Cd source. The experiment has been successfully built and commissioned and the first calibration data in Ar+2%<sup>i</sup>C<sub>4</sub>H<sub>10</sub> have been described in detail. Several changes are planned for a physics run at LSC during 2016, which include a new external support and shielding, the installation of two radiopure Micromegas readouts and the use of a gas without radioactive elements. The implementation of AGET electronics, with auto-trigger functionality, will also reduce the energy threshold from the actual 2.8 keV down to about 100 eV, as first results with other Micromegas detectors have shown.

During the design and construction of TREX-DM, a material screening program (mainly based on germanium gamma-ray spectrometry) was undertaken to evaluate the radioactivity of all the relevant components of the detector and surrounding materials. These results have been used to build a first background model of the experiment, in combination with the full simulation of the detector’s response and an analysis optimized to discriminate point-like events from complex topologies. Based on this first model, background levels around 1 keV<sup>-1</sup> kg<sup>-1</sup> day<sup>-1</sup> are feasible with the actual detector concept. If the energy threshold is also 0.4 keVee or below, TREX-DM could reach higher sensitivity to low-mass WIMPs than many of the current mainstream experiments, and could exclude the *region of interest* invoked by some positive interpretations of some Dark Matter experiments.

**Acknowledgements** We acknowledge the Micromegas workshop of IRFU/SEDI for bulking our readout planes and the *Servicio General de Apoyo a la Investigación-SAI* of the University of Zaragoza for the fabrication of many mechanical components. We also thank D. Calvet from IRFU/SEDI for his help with the AFTER electronics. We acknowledge the support from the European Commission under the European Research Council T-REX Starting Grant ref. ERC-2009-StG-240054 of the IDEAS program of the 7th EU Framework Program, the Spanish Ministry of Economy and Competitiveness (MINECO) under grants FPA2011-24058 and FPA2013-41085-P and the University of Zaragoza under grant JIUZ-2014-CIE-02. F.I. acknowledges the support from the *Juan de la Cierva* program and T.D. from the *Ramón y Cajal* program of MINECO.

## References

1. G. Bertone, D. Hooper, J. Silk, Phys. Rept. **405**, 279 (2005)
2. G. Jungman, M. Kamionkowski, K. Griest, Phys. Rept. **267**, 195 (1996)
3. D.S. Akerib, et al., Phys. Rev. Lett. **112**, 091303 (2014)
4. E. Aprile, et al., Phys. Rev. Lett. **109**, 181301 (2012)
5. Z. Ahmed, et al., Science **327**, 1619 (2010)
6. R. Agnese, et al., Phys. Rev. **D92** (2015)
7. R. Agnese, et al., Phys. Rev. Lett. **112** (2014)

8. A.K. Drukier, S. Nussinov, *Int. J. Mod. Phys. A* **A28**, 1330033 (2013)
9. K.M. Zurek, *Phys. Rept.* **537**, 91 (2014)
10. R. Bernabei, et al., *Eur. Phys. J. C* **73**, 2648 (2013)
11. C.E. Aalseth, et al., *Phys. Rev. D* **88**, 012002 (2013)
12. G. Angloher, et al., *Eur. Phys. J. C* **72**, 1971 (2012)
13. G. Angloher, et al., *Eur. Phys. J. C* **74** (2014)
14. C. Savage, G. Gelmini, P. Gondolo, K. Freese, *JCAP* **0904**, 010 (2009)
15. J. Angle, et al., *Phys. Rev. Lett.* **107**, 051301 (2011)
16. A.E. Chavarria, et al., *Phys. Procedia* **61**, 21 (2015)
17. Q. Yue, et al., *Phys. Rev. D* **90**, 091701 (2014)
18. R. Agnese, et al., Submitted to: *Phys. Rev. Lett.* (2015). [arXiv:1509.02448](https://arxiv.org/abs/1509.02448)
19. I.G. Irastorza, et al., *EAS Publ. Ser.* **53**, 147 (2012)
20. T. Dafni, et al., *J. Phys. Conf. Ser.* **375**, 022003 (2012)
21. S. Aune, et al., *JINST* **9** (2014)
22. S. Cebrian, et al., *JCAP* **1010**, 010 (2010)
23. Y. Giomataris, P. Rebourgeard, J.P. Robert, G. Charpak, *Nucl. Instrum. Meth. A* **376**, 29 (1996)
24. S. Andriamonje, et al., *JINST* **5**, P02001 (2010)
25. S. Cebrian, et al., *Astropart. Phys.* **34**, 354 (2011)
26. S. Cebrián, et al., *J. Phys. G* **40**, 125203 (2013)
27. F. Aznar, et al., *JCAP* **1512**, 008 (2015)
28. V. Álvarez, et al., *JINST* **9**, P03010 (2014)
29. V. Álvarez, et al., *JINST* **9**, C04015 (2014)
30. D. González-Díaz, et al., *Nucl. Instrum. Meth. A* **804**, 8 (2015)
31. S. Ahlen, et al., *Int. J. Mod. Phys. A* **25**, 1 (2010)
32. E. Daw, et al., *Astropart. Phys.* **35**, 397 (2012)
33. D. Santos, et al., *EAS Publ. Ser.* **53**, 25 (2012)
34. K. Nakamura, et al., *PTEP* **2015** (2015)
35. S. Ahlen, et al., *Phys. Lett. B* **695**, 124 (2011)
36. I. Giomataris, et al., *Nucl. Instrum. Meth. A* **560**, 405 (2006)
37. P. Baron, et al., *IEEE Trans. Nucl. Sci.* **55**, 1744 (2008)
38. P. Baron, et al., *IEEE Trans. Nucl. Sci.* **57**, 406 (2010)
39. A. Peiró, Master's thesis, Univ. Zaragoza (2013). <https://zaguan.unizar.es/record/12149/files/TAZ-PFC-2013-573.pdf>
40. J. Xu, et al., *Astropart. Phys.* **66**, 53 (2015)
41. F.J. Iguaz, E. Ferrer-Ribas, A. Giganon, I. Giomataris, *JINST* **7**, P04007 (2012)
42. S. Cebrian, et al., *JINST* **8**, P01012 (2013)
43. F.J. Iguaz, et al., *JINST* **6**, P07002 (2011)
44. F.J. Iguaz, et al., *Nucl. Instrum. Meth. A* **735**, 399 (2014)
45. H. Schindler, S. Biagi, R. Veenhof, *Nucl. Instrum. Meth. A* **624**
46. P. Baron, et al., *IEEE NSS/MIC* **745** (2011)
47. J. Garza, et al., Talk at the MPGD 2015 conference, Trieste, 2015.
48. F. Aznar, et al., *JINST* **8**, C11012 (2013)
49. L.A. Currie, *Anal. Chem.* **40**, 586 (1968)
50. C. Hurtgen, S. Jerome, M. Woods, *Appl. Rad. Isot.* **53**, 45 (2000)
51. S. Agostinelli, et al., *Nucl. Instrum. Meth. A* **506**, 250 (2003)
52. M. Laubenstein, et al., *Appl. Rad. and Isot.* **61**, 167 (2004)
53. S. Cebrián, et al., *JINST* **10**, P05006 (2015)
54. G. Heusser, *Ann. Rev. Nucl. Part. Sci.* **45**, 543 (1995)
55. H. Gómez, *Nucl. Instrum. Meth. A* **718**, 52 (2013)
56. H. Gómez, et al. Radiopurity measurement of microegas readouts and components with the bipo-3 detector. Article in preparation
57. S. Cebrián, et al., *Astropart. Phys.* **37**, 60 (2012)
58. G. Luzon, et al., in *Proceedings, 6th International Workshop on The identification of dark matter (IDM 2006)* (2006), pp. 514–519
59. D.S. Leonard, et al., *Nucl. Instrum. Meth. A* **591**, 490 (2008)
60. P. Agnes, et al., (2015). [arXiv:1510.00702](https://arxiv.org/abs/1510.00702)
61. J.M. Carmona, et al., *Astropart. Phys.* **21**, 523 (2004)
62. O.A. Ponkratenko, V.I. Tretyak, Yu.G. Zdesenko, *Phys. Atom. Nucl.* **63**, 1282 (2000)
63. A. Tomas, Ph.D. thesis, Univ. Zaragoza (2013). [CERN-THESIS-2013-062](https://arxiv.org/abs/1306.0062)
64. S.F. Biagi, *Nucl. Instrum. Meth. A* **421** (1999)
65. J. Billard, F. Mayet, D. Santos, *JCAP* **1207**, 020 (2012)
66. A.B. Smith, P.R. Fields, J.H. Roberts, *Phys. Rev.* **108**, 411 (1957)
67. P.F. Smith, J.D. Lewin, *Phys. Rept.* **187**, 203 (1990)
68. J. Lindhard, M. Scharff, H. Schiott, *Mat. Fys. Medd. Dan. Vid. Selsk.* **33**(14), 1 (1963)
69. W. Creus, Y. Allkofer, C. Amsler, A.D. Ferella, J. Rochet, L. Scotto-Lavina, M. Walter, *JINST* **10**, P08002 (2015)
70. R. Agnese, et al., *Phys. Rev. Lett.* **111**, 251301 (2013)
71. G. Angloher, et al., (2015). [arXiv:1509.01515](https://arxiv.org/abs/1509.01515)